Research Square

Preprints are preliminary reports that have not undergone peer review.
They should not be considered conclusive, used to inform clinical practice,
or referenced by the media as validated information.

Targeting succinate-driven microglial metabolic reprogramming alleviates neuroinflammation after cerebral ischemia–reperfusion

zhuohang Liu
Minhang Hospital
Zengyu Zhang
Minhang Hospital
Kaicheng Yang
Minhang Hospital
Rong Ji
Minhang Hospital
Xueyu Mao
Minhang Hospital
Huicong Niu
Minhang Hospital
Min Chu
Minhang Hospital
Yong Wang
Zhongshan Hospital
Jing Zhao
zhao_jing@fudan.edu.cn

Minhang Hospital

Research Article

Keywords: Ischemic stroke, Succinate, Microglia, SUCNR1 (GPR91), Immunometabolism

Posted Date: June 23rd, 2026

DOI: https://doi.org/10.21203/rs.3.rs-9985262/v1

License: This work is licensed under a Creative Commons Attribution 4.0 International License.
Read Full License

Additional Declarations: No competing interests reported.

Targeting succinate-driven microglial metabolic reprogramming alleviates neuroinflammation after cerebral ischemia–reperfusion

Zhuohang Liu 1,2#, Zengyu Zhang 3#, Kaicheng Yang 1#, Rong Ji1, Xueyu Mao1, Huicong Niu1, Min Chu 4,Yong Wang5*,Jing Zhao1,6*

1Department of Neurology of Minhang Hospital,Fudan University, Shanghai, China;

2Department of Rehabilitation, Zhongshan Hospital, Fudan University, Shanghai, China;

3Department of Neurology of Minhang Hospital, State Key Laboratory of Brain Function and Disorders, MOE Frontiers Center for Brain Science, and Institutes of Brain Science, Fudan University, Shanghai, China;

and Disorders, MOE Frontiers Center for Brain Science, and Institutes of Brain Science, Fudan University, Shanghai, China;

4Department of Geriatrics, Shanghai Geriatric Medical Center, Shanghai 201104, China;

5Department of Neurology, Zhongshan Hospital, Fudan University, Shanghai, China;

6Institute of Healthy Yangtze River Delta, Shanghai Jiao Tong University, Shanghai, China

#The authors contributed equally to this study.

*Corresponding authors:

Jing Zhao (zhao_jing@fudan.edu.cn); Yong Wang (yong_wangchn@163.com)

Abstract

Background:

Ischemic stroke triggers profound metabolic disturbance and oxidative stress following ischemia–reperfusion, driving secondary neuroinflammation and neuronal injury. Succinate rapidly accumulates under ischemic conditions, yet its active role and receptor-mediated mechanisms in post-stroke inflammation remain unclear.

Methods:

We integrated targeted metabolomics, clinical association analyses, and mechanistic studies in mouse ischemia–reperfusion models and primary microglia. Genetic and pharmacological approaches, transcriptomic profiling, and extracellular flux analyses were employed to dissect succinate-mediated signaling pathways. A targeted nanoparticle-based delivery system was used to selectively inhibit succinate metabolism in microglia in vivo.

Results:

Succinate robustly accumulated in ischemic brain tissue and in the circulation of stroke patients, where elevated levels independently predicted poor clinical outcomes. In mice, exogenous succinate aggravated infarct volume, neurological deficits, and neuroinflammation, whereas inhibition of succinate accumulation with malonate conferred significant neuroprotection. Mechanistically, succinate selectively activated microglial succinate receptor 1 (SUCNR1), promoting pro-inflammatory polarization and glycolytic reprogramming. Hypoxia-inducible factor-1α (HIF-1α) was identified as a key downstream effector linking SUCNR1 signaling to metabolic and inflammatory amplification. Genetic or pharmacological disruption of the SUCNR1/HIF-1α axis suppressed microglial inflammation, reduced neuronal apoptosis, and improved functional recovery. Targeted delivery of a succinate metabolism inhibitor further reduced infarct size, neuroinflammation, and neurological deficits in vivo.

Conclusion:

These findings identify succinate as an active immunometabolic signal that amplifies neuroinflammation after ischemic stroke through a microglial SUCNR1–HIF-1α axis, highlighting a therapeutically tractable pathway for neuroprotection and targeted metabolic intervention.

Keywords: Ischemic stroke; Succinate ; Microglia;SUCNR1 (GPR91); Immunometabolism

1.Introduction

Ischemic stroke stands as one of the leading global causes of mortality and long-term disability. Its core pathological cascade is initiated by cerebral blood flow interruption, leading to neuronal energy deprivation and subsequent tissue necrosis. Within this cascade, neuroinflammation emerges as a critical driver of secondary injury, profoundly influencing both acute pathological progression and long-term functional recovery[1–3].

As the resident immune sentinels of the central nervous system, microglia undergo rapid activation following ischemic insult. This activation is characterized by morphological transformation, increased release of inflammatory mediators, and enhanced chemotactic and phagocytic functions. While essential for debris clearance and initiating repair, sustained or dysregulated microglial activation can fuel excessive pathological inflammation, exacerbating tissue damage[4–6]. Substantial evidence links aberrant microglial responses to post-stroke neuronal death, blood-brain barrier disruption, and persistent neurological deficits[7–9].

Recent breakthroughs in the field of immunometabolism have revealed a tight coupling between immune cell functional states and metabolic reprogramming. Metabolic intermediates serve not only as substrates for energy and biosynthesis but also as crucial signaling molecules that directly modulate the intensity and direction of inflammatory responses [10–12]. In the specific context of ischemia/reperfusion injury, mitochondrial dysfunction disrupts the tricarboxylic acid (TCA) cycle, leading to a significant accumulation of the intermediate succinate. This accumulation has been shown to amplify cellular stress and oxidative damage through multiple mechanisms[13–15]. For instance, intracellular succinate accumulation inhibits prolyl hydroxylase activity, thereby stabilizing hypoxia-inducible factor-1α (HIF-1α) and promoting the transcription of a suite of pro-inflammatory genes[16,17]. Intriguingly, emerging research indicates that succinate can be actively transported or passively released into the extracellular space, where it acts as a “metabokine” or metabolic alarm signal, mediating intercellular communication and modulating inflammation within the local microenvironment[18–20].

The primary receptor for extracellular succinate is the succinate receptor 1 (SUCNR1, also known as GPR91), a G protein-coupled receptor. It specifically senses fluctuations in extracellular succinate concentrations and activates downstream Gαi and Gαq signaling pathways, thereby influencing cellular functions[21–23]. Studies demonstrate that SUCNR1 activation can exert diverse, context-dependent effects. In macrophages, for example, SUCNR1 signaling influences polarization states and regulates the expression of key inflammatory cytokines such as IL-1β and TNF-α[24,25]. In disease models including

atherosclerosis, inflammatory bowel disease, and obesity-associated metabolic inflammation, the succinate-SUCNR1 axis has been identified as a key amplifier of inflammation and a pathological regulator[24,26,27].

Notably, following cerebral ischemic injury, succinate levels have been detected to rise rapidly in the ischemic core and penumbra, with the extent of increase correlating positively with the intensity of post-reperfusion oxidative stress and the scale of tissue damage[17,28]. Animal models further confirm that elevated succinate can be sensed by SUCNR1-expressing cells in the brain (including glia, neurons, and vascular endothelial cells), influencing the local inflammatory microenvironment and cellular responses. Although some research suggests a potential role for SUCNR1 signaling in post-ischemic vascular remodeling and angiogenesis[29,30], its specific molecular mechanism in orchestrating the inflammatory phenotype activation of microglia and thereby driving a vicious cycle of neuroinflammation in the context of ischemic stroke remains poorly understood and systematically unelucidated.

Building upon this background and existing knowledge gap, this study aims to investigate whether succinate accumulating after ischemic stroke exacerbates neuroinflammation by activating specific pro-inflammatory signaling pathways (such as NF-κB and MAPK) in microglia via its receptor SUCNR1. We hypothesize that elevated levels of exogenous or local endogenous succinate bind to SUCNR1 on the microglial surface, triggering the activation of downstream classical pro-inflammatory pathways. This cascade promotes a shift of microglia toward a pro-inflammatory phenotype and the robust release of inflammatory mediators, ultimately exacerbating neuronal injury and functional impairment after stroke.By exploring this "metabolite-receptor-inflammation" axis, our research not only seeks to deepen the understanding of post-stroke neuroinflammation from a novel immunometabolic perspective but may also provide a crucial theoretical foundation for developing new neuroprotective strategies targeting the succinate-SUCNR1 signaling pathway.

2. Materials and methods

2.1 Human subjects and clinical sample collection

Patients with acute ischemic stroke were consecutively recruited from Minhang Hospital, Fudan University. Peripheral venous blood samples were collected immediately upon admission. Serum was isolated by centrifugation and stored at −80 °C until analysis. Patients aged ≥18 years with CT/MRI-confirmed acute ischemic stroke who met eligibility criteria for intravenous thrombolysis and had complete baseline NIHSS data were included. Patients with severe hepatic or renal dysfunction, active bleeding or infection, malignancy, pre-stroke disability (mRS ≥2), limited life expectancy, or incomplete follow-up were excluded.Clinical outcome was assessed at 3 months after stroke onset using the modified Rankin Scale (mRS). Patients were classified into a favorable outcome group (mRS ≤ 2) or an unfavorable outcome group (mRS > 2).Informed consent was obtained from all participants. The study was approved by the Institutional Ethics Committee of Minhang Hospital, Fudan University (Approval Number: 2021-008-01K), and all procedures were conducted in accordance with the Declaration of Helsinki.

2.2 Animals

Adult male C57BL/6J mice (8–10 weeks old,22–26 g) were used in this study. Mice were housed under specific pathogen–free conditions with a 12-h light/dark cycle and free access to food and water. Sucnr1−/− mice were generated on a C57BL/6NCya background using a conventional knockout strategy and obtained by intercrossing Sucnr1+/− mice. Genotypes were determined by PCR analysis of tail genomic DNA. The mutant allele was identified by an 824-bp band using F1/R1 primers, whereas the wild-type allele was identified by a 619-bp band using F2/R2 primers. Sucnr1−/− mice were defined as animals carrying the mutant allele without the wild-type allele, and wild-type littermates were used as controls. All experimental procedures complied with the National Institutes of Health (NIH) Guide for the Care and Use of Laboratory Animals and were approved by the Department of Laboratory Animal Science, Fudan University (Approval No. 2023-MHFY-23JZS). Measures were taken to minimize discomfort and distress throughout the study.

2.3 Transient middle cerebral artery occlusion (tMCAO) model

Transient focal cerebral ischemia was induced using the intraluminal filament method. Briefly, mice were anesthetized and a silicone-coated nylon filament was advanced through the external carotid artery to occlude the middle cerebral artery. Occlusion was maintained for 60 min, followed by filament withdrawal to allow reperfusion.

Sham-operated mice underwent the same surgical procedures without filament insertion. Core body temperature was maintained at 37 ± 0.5 °C throughout surgery.

2.4 Cerebral blood flow monitoring

Regional cerebral blood flow (rCBF) was monitored using laser speckle contrast imaging at baseline, 10 min after ischemia onset, and 10 min after reperfusion. Only mice exhibiting a ≥70% reduction in rCBF during ischemia and evident recovery upon reperfusion were included in subsequent analyses.

2.5 Drug administration

2.5.1 Succinate administration

To mimic sustained ischemia-associated metabolic perturbation, mice received intraperitoneal injections of succinate (8 mM/kg) once daily starting 3 days before ischemia and continuing until 3 days after reperfusion. This dosing regimen was adopted from previously published studies and aimed to reproduce pathological succinate accumulation rather than pharmacological overdose.

2.5.2 Disodium malonate (DSM) administration and time-window optimization

DSM, a succinate metabolism inhibitor, was administered via intravenous injection (640 mg/kg) to ensure rapid systemic availability.

To determine the optimal therapeutic window, DSM was administered at three distinct time points:

1. Pre-ischemic phase: 30–10 min before ischemia;
2. Ischemic phase: from 50 min after ischemia onset to 10 min after reperfusion;
3. Early reperfusion phase: 10–30 min after reperfusion.

Based on infarct volume and neurological outcome assessments, ischemic-phase administration was identified as the most effective intervention. All subsequent mechanistic and therapeutic experiments were therefore performed using this predefined optimal time window.

2.6 Tissue collection and infarct assessment

At designated time points after reperfusion, mice were euthanized and brains were harvested. Infarct core and peri-infarct regions were identified based on anatomical landmarks and TTC staining. Tissues were processed for metabolomic, biochemical, histological, and molecular analyses.

2.7 Targeted Metabolomic Analysis

Targeted metabolomic analysis was conducted by Majorbio (Shanghai, China). Tissue samples were extracted under cold conditions using an internal standard–containing solvent, followed by centrifugation to obtain the supernatant. Metabolites were derivatized with 3-NPH and EDC to enhance detection sensitivity and subsequently analyzed using an LC–MS/MS system (UHPLC coupled to a triple quadrupole mass spectrometer). Chromatographic separation was achieved on a reversed-phase column, and metabolites were detected in multiple reaction monitoring (MRM) mode. Quantitative analysis was performed using isotopically labeled internal standards and external calibration curves, with metabolite abundances normalized to sample weight and dilution factors.

2.8 RNA Extraction and RT-qPCR

Total RNA was extracted from mouse brain tissues or cultured microglia and reverse-transcribed into cDNA. Quantitative real-time PCR was performed using SYBR Green chemistry with GAPDH as the internal reference gene. Relative gene expression levels were calculated using the 2^−ΔΔCt method, and all experiments were conducted with at least three independent replicates. All primer sequences used for RT-qPCR analysis are provided in Supplementary Table 1.

2.9 Transwell Migration Assay

Microglial migratory capacity was evaluated using a Transwell chamber system. Cells were seeded into the upper chamber, while the lower chamber contained serum-supplemented medium as a chemoattractant. After incubation, migrated cells on the lower surface of the membrane were fixed, stained, and quantified in randomly selected fields.

2.10 Flow Cytometry Analysis

For phagocytosis assays, microglia were incubated with fluorescently labeled latex beads, washed thoroughly, and analyzed by flow cytometry to determine the percentage of phagocytic cells. For phenotypic characterization, cells were stained with fluorophore-conjugated antibodies against CD86 and CD206 to assess inflammatory polarization, with isotype controls used to define gating strategies. Cell apoptosis was evaluated using Annexin V-FITC/PI staining followed by flow cytometric analysis.

2.11 Primary Microglia Isolation and Culture

Primary microglia were isolated from neonatal or adult mice as described previously[31]. Neonatal mouse brains were used to establish mixed glial cultures, from which microglia were obtained after differential detachment and validated by Iba1 immunostaining. For adult mice, brain tissues were enzymatically dissociated, and microglia were enriched using CD11b-based magnetic-activated cell sorting for subsequent experiments.

2.12 Microglial stimulation and conditioned-medium treatment of HT22 cells

Primary microglia or BV2 cells were treated with LPS (100 ng/mL) for 24 h in the presence or absence of succinate (4 mM), DSM (5 mM), DMOG (200 μM), or PX-478 (10 μM). The treated cells were then subjected to subsequent analyses, including immunofluorescence

staining, qPCR, Western blotting, ELISA, Seahorse assays, and conditioned-medium experiments. For conditioned-medium experiments, primary microglia were seeded in 6-well plates and stimulated with LPS with or without DSM for 24 h. The culture supernatants were collected as microglia-conditioned medium. HT22 cells were subsequently incubated with a 1:1 mixture of microglia-conditioned medium and fresh high-glucose DMEM for 24 h, followed by assessment of reactive oxygen species production, mitochondrial function, and apoptosis.

2.13 Immunofluorescence staining and Western blot analysis

Brain sections were incubated with primary antibodies against Iba1, Sucnr1, CD16, iNOS, Arg1, NeuN, and GFAP, followed by appropriate fluorophore-conjugated secondary antibodies. Nuclei were counterstained with DAPI. The primary antibody against Sucnr1 was obtained from Novus Biologicals (NBP1-00861) and used at a dilution of 1:200 for immunofluorescence (IF) and 1:1000 for Western blot (WB). All other primary antibodies for immunofluorescence were used at a dilution of 1:500, and all primary antibodies for Western blotting were used at a dilution of 1:1000.The antibodies used for immunofluorescence included goat anti-Iba1 (Abcam, ab5076), rabbit anti-Iba1 (Abcam, ab178846), chicken anti-GFAP (Abcam, ab4674), mouse anti-NeuN (Sigma-Aldrich, MAB377A5), rabbit anti-NeuN (Abcam, ab177487), rat anti-CD16 (BD Biosciences, 553142), rabbit anti-iNOS (Cell Signaling Technology, 13120S), and rabbit anti-HIF-1α (Abcam, ab179483).For Western blot analysis, primary antibodies included rabbit anti-iNOS (Cell Signaling Technology, 13120S), rabbit anti-PKM2 (Proteintech, 15822-1-AP), and rabbit anti-HIF-1α (Cell Signaling Technology, 36169T). Microglial morphology was quantitatively assessed using Sholl analysis as previously described[32].

2.14 RNA sequencing and bioinformatic analysis

RNA sequencing was performed by Tianjin Gene Wisdom Biotechnology Co., Ltd. Differential expression analysis, Mfuzz clustering, GO enrichment, and GSEA were conducted using R software (version 4.4). Genes with $|\log_2 FC| > 1$ and adjusted $P < 0.05$ were considered differentially expressed.

2.15 Seahorse metabolic flux analysis

Extracellular acidification rate (ECAR) and oxygen consumption rate (OCR) were measured using a Seahorse XF Analyzer to assess glycolytic activity and mitochondrial respiration in microglia.

2.16 Preparation and evaluation of the nanoparticle delivery system

Mesoporous silica nanoparticles were synthesized and sequentially functionalized to construct a targeted drug delivery system. Briefly, amine-modified mesoporous silica nanoparticles were prepared and subsequently loaded with DSM. For targeted delivery, RGD peptides were further conjugated to generate RGD-functionalized, DSM-loaded nanoparticles (MNDR). The obtained nanoparticles were purified and used for subsequent in vitro and in vivo experiments.The biocompatibility of nanoparticles was evaluated in microglial cells using a Cell Counting Kit-8 (CCK-8) assay. Cellular uptake was assessed by incubating cells with Cy5-labeled nanoparticles, followed by nuclear counterstaining and confocal laser scanning microscopy. Microglial metabolic reprogramming and inflammatory responses were analyzed using Seahorse extracellular flux analysis and ELISA, respectively, as described above. For in vivo distribution analysis, mice subjected to

cerebral ischemia–reperfusion injury were sacrificed at the indicated time point, and intact brains were collected for ex vivo fluorescence imaging. Cy5 fluorescence signals were acquired using an IVIS Spectrum imaging system and reconstructed to visualize the spatial distribution of nanoparticles within brain tissue.

2.17 Behavioral assessments

Neurological function was evaluated using Garcia score, rotarod test, adhesive removal test, and open-field test at 1, 3, 7, 14, and 28 days after reperfusion[33,34]. All assessments were performed in a blinded manner.

2.18 Statistical analysis

Data are presented as mean ± SEM. Statistical analyses were performed using Student's *t*-test or one- or two-way ANOVA followed by Tukey's post hoc test. Multivariable logistic regression was used for clinical outcome analyses. $P < 0.05$ was considered statistically significant.

3.Results

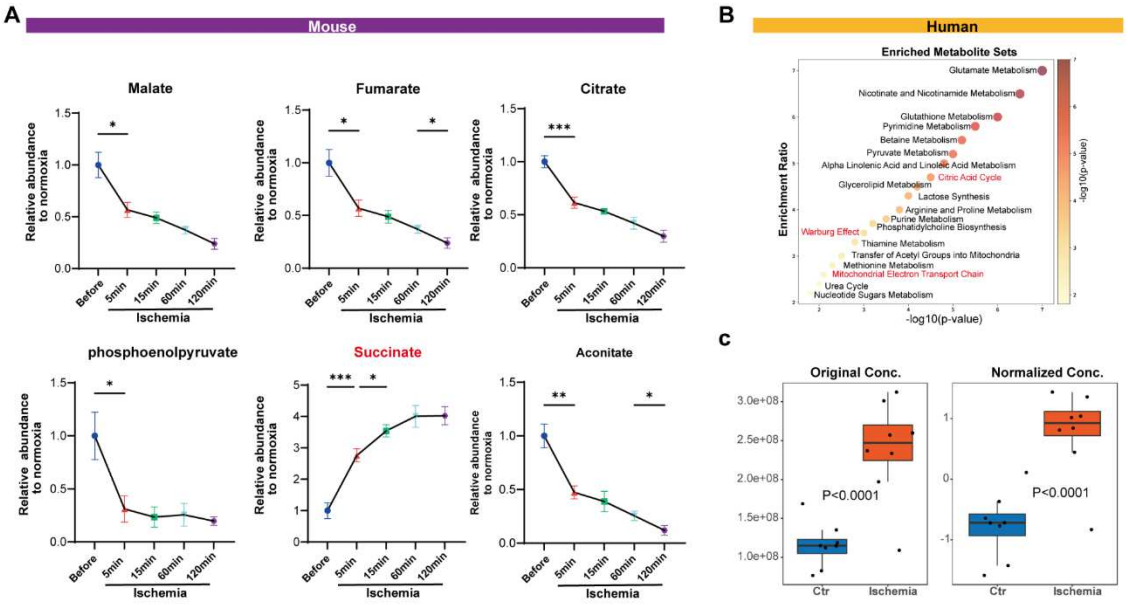
Succinate Accumulation: A Prognostic Metabolic Marker in Ischemic Stroke

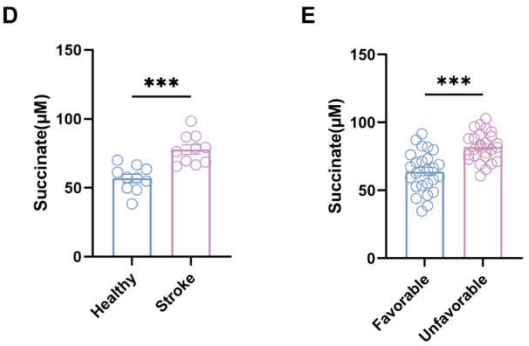
To investigate the role of metabolic dysregulation in the pathogenesis of ischemic stroke, we first performed an exploratory analysis based on a published dataset derived from a human brain warm ischemia model [35]. In this dataset, differential metabolites after warm ischemia were significantly enriched in the tricarboxylic acid (TCA) cycle and related pathways, with a marked elevation of succinate levels (Fig.1b,c and Fig.1S). These findings suggest that succinate accumulation may represent a key pathological metabolic event following stroke. Consistently, our time-course analysis in a mouse model showed widespread perturbation of TCA cycle intermediates during ischemia–reperfusion, among which the rapid early accumulation of succinate was particularly prominent (Fig.1a).Building on the concordant changes in succinate observed in both human tissue and animal models, we next validated its clinical relevance in an independent patient cohort. We found that serum succinate levels in patients with acute ischemic stroke were significantly higher than those in healthy controls (Fig.1d), and that patients with poor outcomes had substantially higher succinate concentrations than those with favorable outcomes (Fig.1e). Multivariable regression analysis confirmed succinate as an independent risk factor for adverse prognosis (Fig.1f). Furthermore, by constructing a stratified logistic regression model based on succinate concentration, we demonstrated that elevated succinate levels were strongly associated with an increased risk of poor clinical outcome (Fig.1g), supporting its potential as a prognostic biomarker.

To mechanistically delineate the direct pathogenic role of succinate accumulation, we established a middle cerebral artery occlusion (MCAO) model in mice. Using laser speckle imaging, we dynamically monitored changes in local cortical cerebral blood flow at baseline, during ischemia, and after reperfusion (Fig. 1h). We then precisely dissected tissue from the infarct core (Fig. 1i) and performed targeted metabolomic profiling by LC–MS/MS. The resulting heatmap revealed broad disturbances in several TCA intermediates in ischemic brain tissue compared with sham controls, with succinate showing the most pronounced accumulation (Fig. 1j). Finally, we measured levels of malonate, a competitive inhibitor of succinate metabolism, and found that malonate and succinate displayed opposite trends after ischemia–reperfusion (Fig. 1k), further supporting a stroke-induced, pathway-specific

imbalance in succinate metabolism.

Taken together, our data show that succinate accumulation after ischemic stroke is a conserved pathological feature tightly linked to clinical outcome, and that its disrupted metabolism acts as a key driver of ischemic brain injury.





F

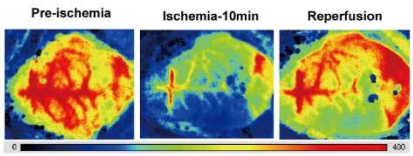
Characteristic	OR(adjusted)
Sex	0.37 (0.06-2.31, p=0.286)
Age,y	1.24 (1.09-1.4, p<0.001)
NIHSS	1.26 (1.03-1.53, p=0.024)
Smoking	2.65 (0.25-27.87, p=0.418)
Hypertension	2.97 (0.48-18.54, p=0.243)
TOAST	
LAA	Reference
SAO	0.09 (0.01-1, p=0.050)
CE	0.26 (0.02-3.44, p=0.310)
Others	0 (0-Inf, p=0.994)
Diabetes	0.23 (0.02-2.24, p=0.204)
Fasting blood glucose (mmol/L)	1.4 (1-1.97, p=0.053)
Succinate (μmol/L)	1.08 (1.03-1.14, p=0.004)

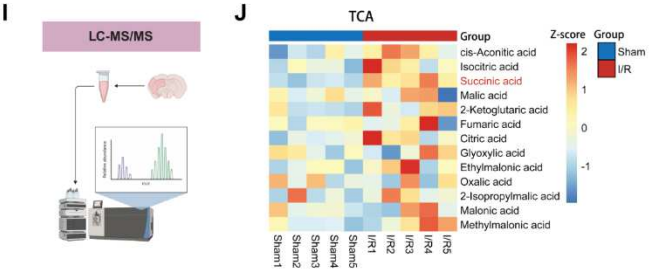
G

Characteristic	Model 1			Model 2			Model 3		
	OR[1]	95% CI[1]	p-value	OR[1]	95% CI[1]	p-value	OR[1]	95% CI[1]	p-value
Succinate (μmol/L) (continuous)	1.04	1.02, 1.07	<0.001	1.08	1.03, 1.12	<0.001	1.08	1.03, 1.14	0.004
Succinate(μmol/L) (standardized)	2.53	1.48, 4.30	<0.001	4.96	2.00, 12.32	<0.001	5.64	1.76, 18.11	0.004
Succinate(μmol/L)									
(Q1:21-34.8)	—	—		—	—		—	—	
(Q2:35.1-54)									
(Q3:54-119.7)									
P for trend			<0.001			0.002			0.004

[1]OR = Odds Ratio, CI = Confidence Interval

Model 1 : no covariates were adjusted
Model 2 : adjusted for Sex and Age
Model 3 : adjusted for Sex, Age, NIHSS, Smoking, Hypertension, TOAST, Diabetes, and Fasting blood glucose





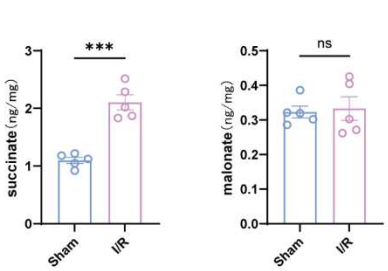


Figure 1. Ischemic stroke induces succinate accumulation and TCA cycle remodeling.

(a) Line plots showing the temporal dynamics of key metabolites in the tricarboxylic acid (TCA) cycle at different time points.

(b) Pathway enrichment analysis of differentially expressed metabolites in human brain tissues under a warm ischemia model.

(c) Changes in succinate levels in human brain tissues subjected to warm ischemic conditions (data from Mottahedin A et al., Redox Biology, 2023).

(d) Circulating succinate levels are significantly elevated in stroke patients compared with healthy controls.

(e) Patients with poor outcomes exhibit markedly higher succinate levels.

(f) Forest plot of clinical variables, including succinate, demonstrating that elevated succinate is strongly associated with unfavorable clinical outcomes.

(g) A stratified logistic regression model based on succinate tertiles was constructed to assess its predictive value for clinical prognosis.

(h) Laser speckle contrast imaging was used to monitor changes in regional cerebral blood flow (rCBF) at multiple time points, including baseline (pre-surgery), 10 min after ischemia onset, and 10 min after reperfusion.

(i) Schematic diagram of the sampling region (the infarct core/penumbra) in the cerebral infarction model for LC-MS/MS analysis(by BioRender).

(j) Heatmap showing the relative abundance of TCA cycle metabolites in the ischemic and sham groups, with Z-score–based color scaling. Succinate levels are significantly elevated in the ischemia–reperfusion group.

(k) Bar graphs indicating changes in succinate and malonate (a succinate inhibitor) levels (n = 5).Data are presented as mean ± SEM unless otherwise indicated. Statistical analyses were performed using one-way or two-way ANOVA followed by Tukey's post hoc test. *$p < 0.05$, **$p < 0.01$, ***$p < 0.001$.

Succinate causally exacerbates ischemic brain injury and neurological dysfunction

By evaluating the therapeutic effects of sodium malonate administration at different time windows, we found that treatment during the ischemic phase most effectively reduced infarct volume and improved neurological deficits, thereby identifying the optimal window for intervention targeting succinate accumulation(Fig.S2).After confirming the marked accumulation of succinate following ischemic stroke, we further investigated its causative role and underlying mechanisms in ischemic brain injury by exogenously supplementing succinate and inhibiting its accumulation with malonate. Targeted metabolomic analysis showed that, compared with the ischemia–reperfusion (I/R) group, the exogenous succinate-treated group exhibited a further increase in brain succinate levels, whereas treatment with the succinate dehydrogenase inhibitor malonate effectively blocked this accumulation (Fig.2a).

To evaluate the impact of succinate on neurological function, a series of long-term behavioral assessments were performed. Ischemia–reperfusion severely impaired sensorimotor function, as reflected by worsened Garcia scores, reduced rotarod endurance, and prolonged adhesive detection and removal times (Fig.2b–e). Exogenous succinate administration significantly exacerbated these deficits and impeded functional

recovery, whereas malonate treatment resulted in the mildest impairments and the most favorable recovery trend (Fig. 2b–e). Consistently, open field testing on day 7 post-stroke revealed a marked reduction in total distance traveled in the succinate-treated mice, indicating more severe impairment of spontaneous locomotor activity (Fig.2f).

At the histopathological level, hematoxylin–eosin and Nissl staining demonstrated pronounced structural disruption and neuronal loss following I/R injury. These pathological changes were aggravated by succinate treatment but substantially alleviated by malonate administration (Fig.2g,h). In parallel, TTC staining revealed that succinate significantly increased infarct volume, whereas malonate effectively reduced the infarcted area (Fig.2i,k).

To further elucidate the mechanisms by which succinate exacerbates injury, we focused on neuroinflammation and microglial function. Immunofluorescence staining showed that microglia engulfed myelin debris after I/R; however, succinate treatment markedly increased the fluorescence intensity of myelin basic protein within microglia, suggesting aberrantly enhanced phagocytic activity or inflammatory responses (Fig.2j,l). Moreover, ELISA and Western blot analyses revealed that succinate significantly upregulated the levels of pro-inflammatory cytokines, including IL-1β, IL-6, and TNF-α (Fig.2m), and increased the protein expression of IL-1β (Fig.2n), whereas malonate effectively suppressed these inflammatory responses.In summary, succinate is not merely a bystander of ischemic stroke but a key pathogenic driver that exacerbates neurological deficits, expands infarct volume, and amplifies neuroinflammation, while inhibition of its accumulation confers robust neuroprotection.

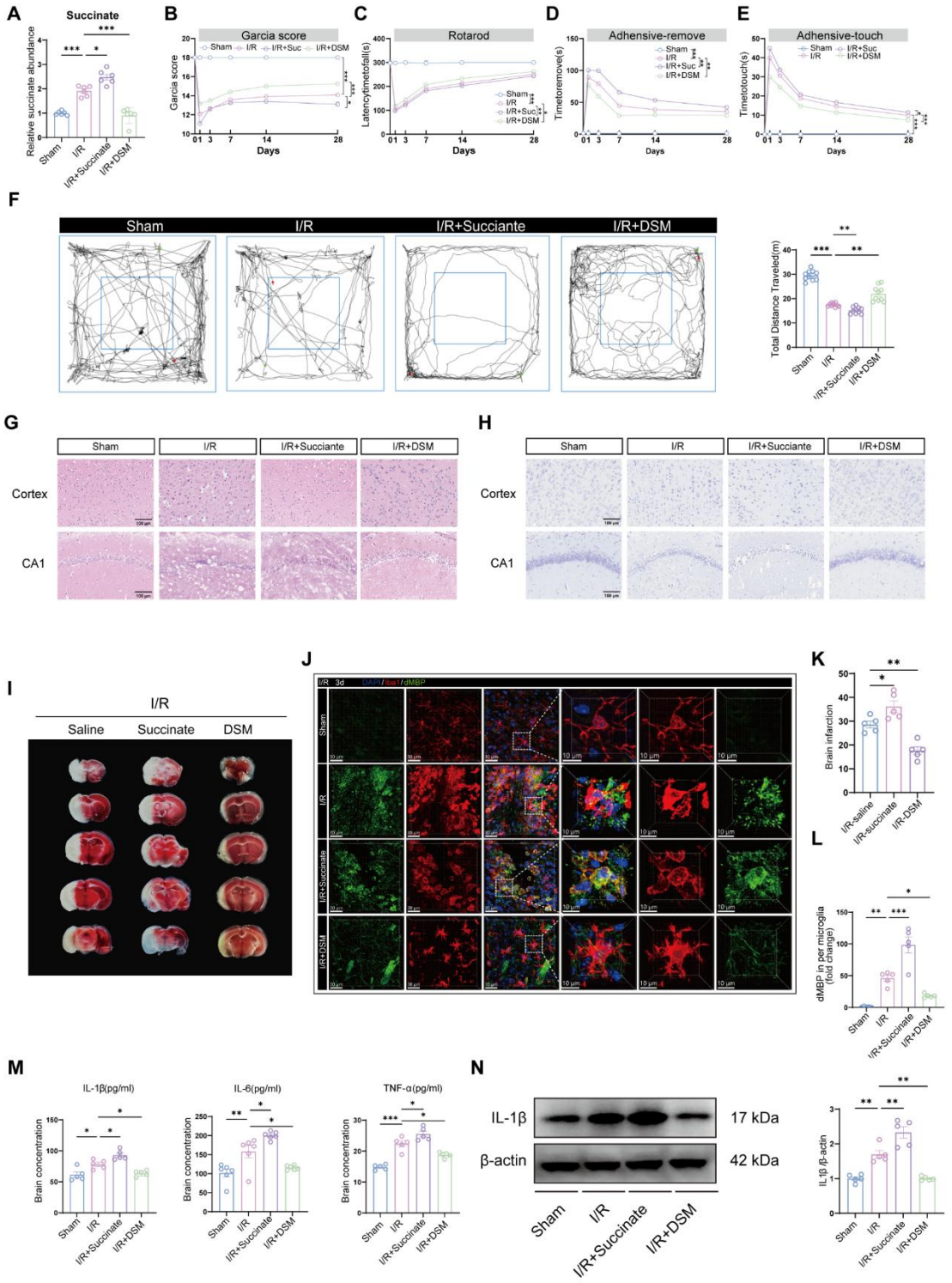


Figure 2. Succinate aggravates ischemic brain injury and neurological dysfunction after stroke.

(a) Targeted metabolomic analysis of succinate levels in brain tissues under different interventions (n = 5).

(b–e) Sensorimotor function was assessed using the Garcia score **(b)**, rotarod test **(c)**, and adhesive removal tests, including adhesive touch **(d)** and adhesive removal **(e)**, on days 1, 3, 7, 14, and 28 after ischemia/reperfusion (n = 10–12).

(f) Open-field test was performed to evaluate locomotor activity on day 7 after stroke, and

total distance traveled (meters) was quantified in each group (n = 10 per group).
(g, h) Representative hematoxylin and eosin (H&E) staining and Nissl staining of paraffin-embedded brain sections illustrating tissue morphology and neuronal survival, with a scale bar of 100 μm.
(i) On day 3 after I/R, 2,3,5-triphenyltetrazolium chloride (TTC) staining was used to visualize infarcted areas (white regions), along with representative images.
(j) Immunofluorescence images showing microglial phagocytosis of myelin debris (dMBP) in different groups. Scale bar = 30 μm; right panels show higher magnification views (scale bar = 10 μm).
(k)quantitative analysis of infarct volume.
(l) Quantification of dMBP fluorescence intensity in each group.
(m) ELISA measurements of inflammatory cytokines IL-1β, IL-6, and TNF-α in brain tissue during the acute phase following I/R.
(n) Western blot analysis of IL-1β expression in brain tissues from each group, along with densitometric quantification of band intensities (n = 5 per group). Sham = sham-operated group; I/R = ischemia–reperfusion group; I/R + succinate = ischemia–reperfusion with succinate treatment; I/R + DSM = ischemia–reperfusion with sodium malonate treatment. Data are presented as mean ± SEM. Statistical analyses were performed using one-way or two-way ANOVA followed by Tukey's post hoc test. *p < 0.05, **p < 0.01, ***p < 0.001.

Succinate skews microglial polarization toward a pro-inflammatory phenotype after stroke

To further delineate the cellular mechanisms by which succinate amplifies neuroinflammation, we next examined its regulatory effects on microglial M1/M2 polarization during the acute phase of stroke. In vivo immunofluorescence staining revealed that, compared with the sham group, ischemia–reperfusion injury markedly drove microglial polarization toward a pro-inflammatory M1 phenotype, as indicated by increased CD16 expression, while simultaneously suppressing the anti-inflammatory M2 phenotype, as reflected by reduced Arg1 expression. Exogenous succinate supplementation further exacerbated this polarization imbalance, significantly enhancing the fluorescence intensity of M1-like marker CD16 and diminishing the expression of M2-like marker Arg1. In contrast, inhibition of succinate accumulation by malonate effectively reversed this trend and promoted a shift of microglia toward the M2 phenotype (Fig.3a,c-d).

To verify the direct effect of succinate on microglial polarization, an in vitro inflammatory model was established using lipopolysaccharide (LPS). Immunofluorescence analysis showed that, compared with the control group, LPS stimulation markedly induced the expression of M1-like marker iNOS. Co-treatment with succinate upon LPS exposure further amplified iNOS expression while concomitantly suppressing the M2 marker Arg1. Conversely, the addition of malonate (DSM) effectively counteracted the effects of succinate and promoted polarization toward the M2 phenotype (Fig.3b,e–h).

To define the molecular basis of DSM-mediated protection, we next performed transcriptomic profiling in LPS-treated microglia. RNA-seq showed that DSM profoundly reprogrammed the LPS-induced transcriptional state, shifting microglia away from inflammatory activation and suppressing pathways linked to hypoxic stress, cellular stress responses, and inflammation. Consistently, GO analysis revealed that DSM predominantly

attenuated ROS metabolic processes, IL-6 and TNF production, innate immune activation, and neuron death-related programs, supporting a role for DSM in restraining metabolism-coupled inflammatory transcriptional programs(Fig.S3a-d). At the functional level, DSM mitigated LPS-induced mitochondrial injury and oxidative stress, restored mitochondrial oxidative phosphorylation, and was associated with increased TOM20 expression, reduced ROS accumulation, and improved basal and maximal respiration(Fig.S3f-n). Consistent with this microglial reprogramming, conditioned medium from DSM-treated microglia alleviated neuronal mitochondrial injury and apoptosis induced by LPS-activated microglia, supporting a role for DSM in limiting the spread of a neurotoxic inflammatory milieu (Fig.S4).

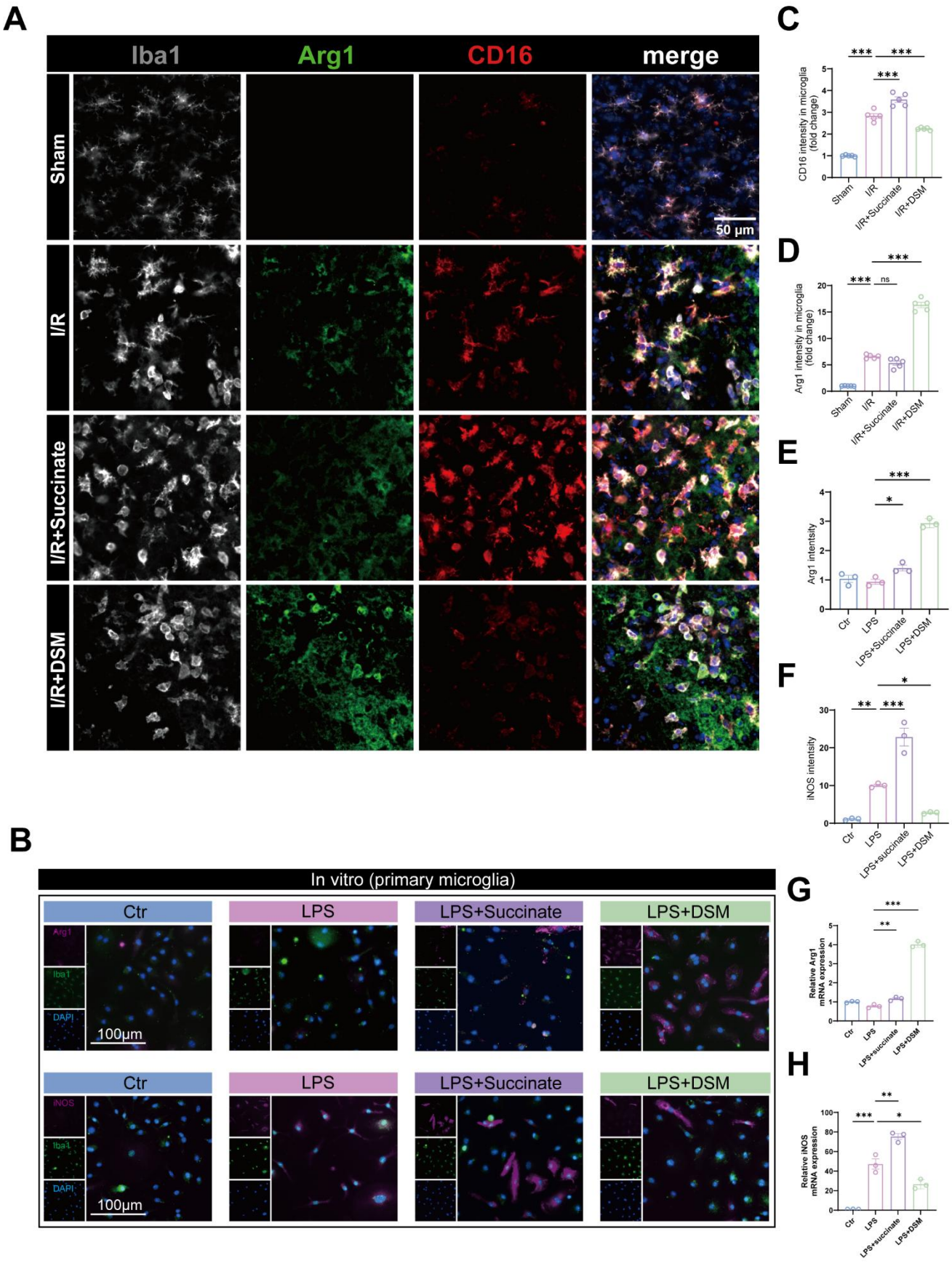


Figure 3. Succinate modulates M1/M2 polarization of microglia after acute stroke.

(a) Representative immunofluorescence images showing expression of M1-like marker (CD16)and M2-like (Arg1) in microglia from different experimental groups.
(b) In vitro immunofluorescence staining of primary microglia showing M2-like (Arg1) and M1-like marker (iNOS) in the Ctrl, LPS, LPS + succinate, and LPS + DSM groups.
(c, d) Quantification of fluorescence intensities of M1-like marker (CD16) and M2-like (Arg1) markers in microglia across groups (n = 5).
(e, f) Quantitative analysis of fluorescence intensities of Arg1 and iNOS in each treatment group (n = 3).
(g, h) qPCR analysis of Arg1 and iNOS in the different groups(n=3).Data are presented as mean ± SEM. Statistical analyses were performed using one-way ANOVA followed by Tukey's post hoc test. ns = not significant, *p < 0.05, **p < 0.01, ***p < 0.001.

Microglial Sucnr1 is selectively upregulated after stroke and mediates ischemic neurotoxicity

Given that succinate can directly regulate microglial polarization, we hypothesized that its specific receptor, Sucnr1, may play a pivotal role in this process. We first examined the expression and distribution of Sucnr1 after stroke. Immunofluorescence staining showed that in the sham group, Sucnr1 exhibited only weak colocalization with the microglial marker Iba1 in both the cortex and striatum. However,by day 3 after ischemia–reperfusion, Sucnr1 fluorescence intensity was markedly increased in ipsilateral cortical and striatal microglia (Fig.4a–d), indicating that acute stroke selectively upregulates microglial Sucnr1. This specificity was corroborated by the lack of significant Sucnr1 expression changes in neurons or astrocytes on the ipsilateral side (Fig.S5a-d).We next sought to determine whether Sucnr1 induction in microglia was associated with ischemia-like stress or inflammatory stimulation. Western blotting and quantitative real-time PCR analyses showed that Sucnr1 expression did not differ significantly between control microglia and cells subjected to OGD/R, consisting of 3 h oxygen–glucose deprivation followed by 24 h reoxygenation (Fig.S5e,g). In contrast, LPS stimulation markedly upregulated Sucnr1 expression in microglia (Fig.S5f,h). Together, these findings suggest that microglial Sucnr1 upregulation after stroke is unlikely to represent a nonspecific response to ischemia-like injury, but may instead be preferentially driven by inflammatory cues.

To further define the functional role of Sucnr1 in stroke pathology, we employed Sucnr1 knockout ($Sucnr1^{-/-}$) mice. Open field testing on day 7 showed that $Sucnr1^{-/-}$ stroke mice traveled a significantly greater total distance than their wild-type counterparts (Fig.4e,f), indicating milder impairment of spontaneous locomotor activity. Consistently, across a series of long-term sensorimotor assessments—including Garcia scores, rotarod performance, and adhesive removal tests—Sucnr1 deficiency was associated with less severe neurological deficits and more rapid functional recovery at all examined time points (Fig.4g–j).At the cellular level, TUNEL/NeuN co-staining revealed that ischemia–reperfusion induced substantial neuronal apoptosis, whereas $Sucnr1^{-/-}$ mice displayed a markedly lower proportion of TUNEL-positive neurons among NeuN-positive cells (Fig.4k,l), indicating that loss of Sucnr1 effectively mitigates ischemia-induced neuronal death. A comparable reduction in neuronal TUNEL positivity was also detected in the striatum, suggesting that the protective effect of Sucnr1 deletion was not restricted to the ischemic cortex but extended across the injured brain region(Fig.S6).Taken together with the

selective upregulation of microglial Sucnr1 after ischemic stroke, these findings demonstrate that Sucnr1 is a critical mediator of neurotoxicity and a key determinant of stroke outcome.

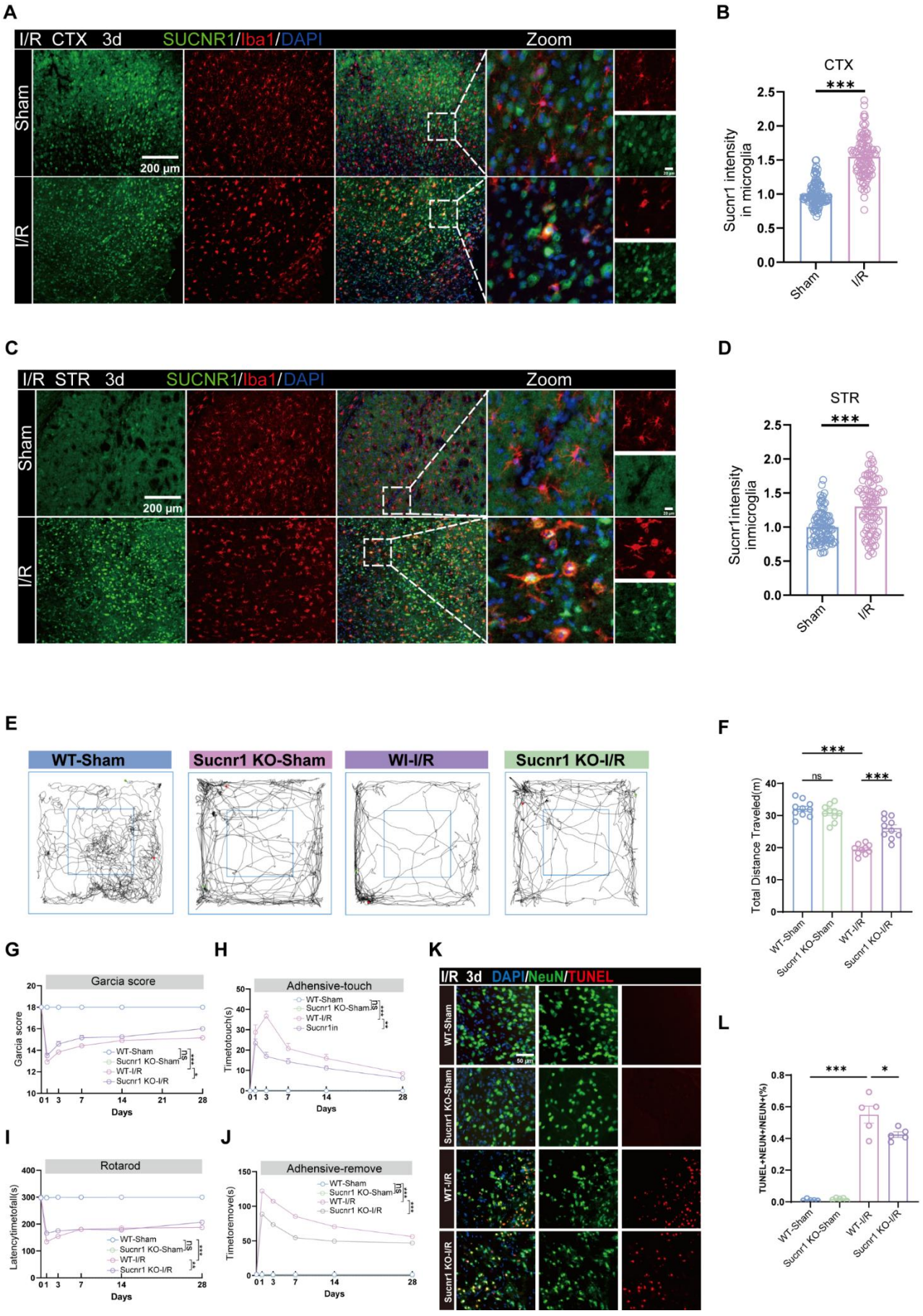

A
I/R CTX 3d
SUCNR1/Iba1/DAPI
Zoom
Sham
I/R
200 μm
B
CTX
***
Sucnr1 intensity in microglia
Sham
I/R
C
I/R STR 3d
SUCNR1/Iba1/DAPI
Zoom
Sham
I/R
200 μm
D
STR
***
Sucnr1intensity inmicroglia
Sham
I/R
E
WT-Sham
Sucnr1 KO-Sham
WI-I/R
Sucnr1 KO-I/R
F
***
ns
***
Total Distance Traveled(m)
WT-Sham
Sucnr1 KO-Sham
WT-I/R
Sucnr1 KO-I/R
G
Garcia score
Garcia score
WT-Sham
Sucnr1 KO-Sham
WT-I/R
Sucnr1 KO-I/R
Days
H
Adhensive-touch
Timetotouch(s)
WT-Sham
Sucnr1 KO-Sham
WT-I/R
Sucnr1in
Days
I
Rotarod
Latencytimetofall(s)
WT-Sham
Sucnr1 KO-Sham
WT-I/R
Sucnr1 KO-I/R
Days
J
Adhensive-remove
Timetoremove(s)
WT-Sham
Sucnr1 KO-Sham
WT-I/R
Sucnr1 KO-I/R
Days
K
I/R 3d DAPI/NeuN/TUNEL
WT-Sham
Sucnr1 KO-Sham
WT-I/R
Sucnr1 KO-I/R
50 μm
L
***
*
TUNEL+NEUN+/NEUN+(%)
WT-Sham
Sucnr1 KO-Sham
WT-I/R
Sucnr1 KO-I/R

Figure 4. Microglial Sucnr1 is selectively upregulated after acute stroke, and its deletion attenuates neurological injury.

(a, c) Representative immunofluorescence images showing colocalization of Sucnr1 with the microglial marker Iba1 in the cortex (a) and striatum (c) of Sham and I/R mice. Low- and high-magnification views are shown, with scale bars = 200 μm and 20 μm, respectively.

(b, d) Quantification of Sucnr1 fluorescence intensity in microglia within the ipsilateral cortex (b) and striatum (d) at day 3 after I/R (n > 50 cells per group).

(e) Open-field test assessing the effect of Sucnr1 deletion ($Sucnr1^{-/-}$) on locomotor activity at day 7 after acute ischemic stroke.

(f) Quantitative analysis of total distance traveled in the open field (meters) in each group (n = 10 per group).

(g–j) Sensorimotor performance was evaluated using the Garcia score (g), rotarod test (h), and adhesive tests, including adhesive touch (i) and adhesive removal (j), on days 1, 3, 7, 14, and 28 after surgery to determine the impact of Sucnr1 deficiency on functional recovery.

(k) Immunofluorescence staining of the ipsilateral cortex showing colabeling of the neuronal marker NeuN (green) and the apoptosis marker TUNEL (red) to assess neuronal apoptosis. Scale bar = 50 μm.

(l) Quantification of the proportion of apoptotic neurons ($NeuN^{+}/TUNEL^{+}$) in each group (n = 5 per group).Data are presented as mean ± SEM. Statistical analyses were performed using one-way or two-way ANOVA followed by Tukey's post hoc test. ns = not significant,*p < 0.05, **p < 0.01, ***p < 0.001.

Sucnr1 regulates microglial functional states after ischemic stroke

To elucidate the cellular mechanisms underlying the neuroprotection conferred by Sucnr1 deficiency, we focused on its regulatory effects on microglial function. Microglial morphology was first assessed by immunofluorescence staining combined with Sholl analysis. Compared with wild-type (WT) stroke mice, microglia in the ipsilateral cortex of $Sucnr1^{-/-}$ stroke mice exhibited significantly longer processes and a more complex branching pattern (Fig.5a–c). This ramified morphology more closely resembled a surveillant, homeostatic state, indicating an altered activation profile in the absence of Sucnr1.We next examined microglial polarization. Immunofluorescence analysis revealed that, in $Sucnr1^{-/-}$ stroke mice, microglial polarization toward the pro-inflammatory M1 phenotype ($CD16^{+}$) was markedly suppressed, whereas polarization toward the anti-inflammatory M2 phenotype ($Arg1^{+}$) was significantly enhanced (Fig.5d–g). In parallel, analysis of the peri-infarct cortex demonstrated that Sucnr1 deficiency substantially reduced microglial proliferation, as evidenced by a decreased number and proportion of $pH3^{+}$ and $Ki67^{+}$ proliferating microglia (Fig.5h–m). These findings suggest that Sucnr1 signaling not only governs microglial phenotype but also contributes to their proliferative response under ischemic conditions.

To confirm these phenotypic changes at the molecular level and determine direct effects, we employed an in vitro model in which primary microglia were stimulated with LPS following Sucnr1 knockdown. qPCR analysis showed that under inflammatory conditions, Sucnr1 silencing significantly reduced the mRNA expression of key pro-inflammatory

cytokines (IL-6, IL-1β, and TNF-α) (Fig.5n), concomitantly downregulated M1-associated markers (CD32, iNOS), and upregulated M2-associated markers (CD206, Arg1) Fig.5o). Consistent with these findings, Western blot analysis further confirmed that Sucnr1 knockdown effectively attenuated LPS-induced iNOS and IL-1β protein expression (Fig.5p–s). Collectively, these in vitro results establish Sucnr1 as a direct and critical regulator of microglial inflammatory activation and polarization.

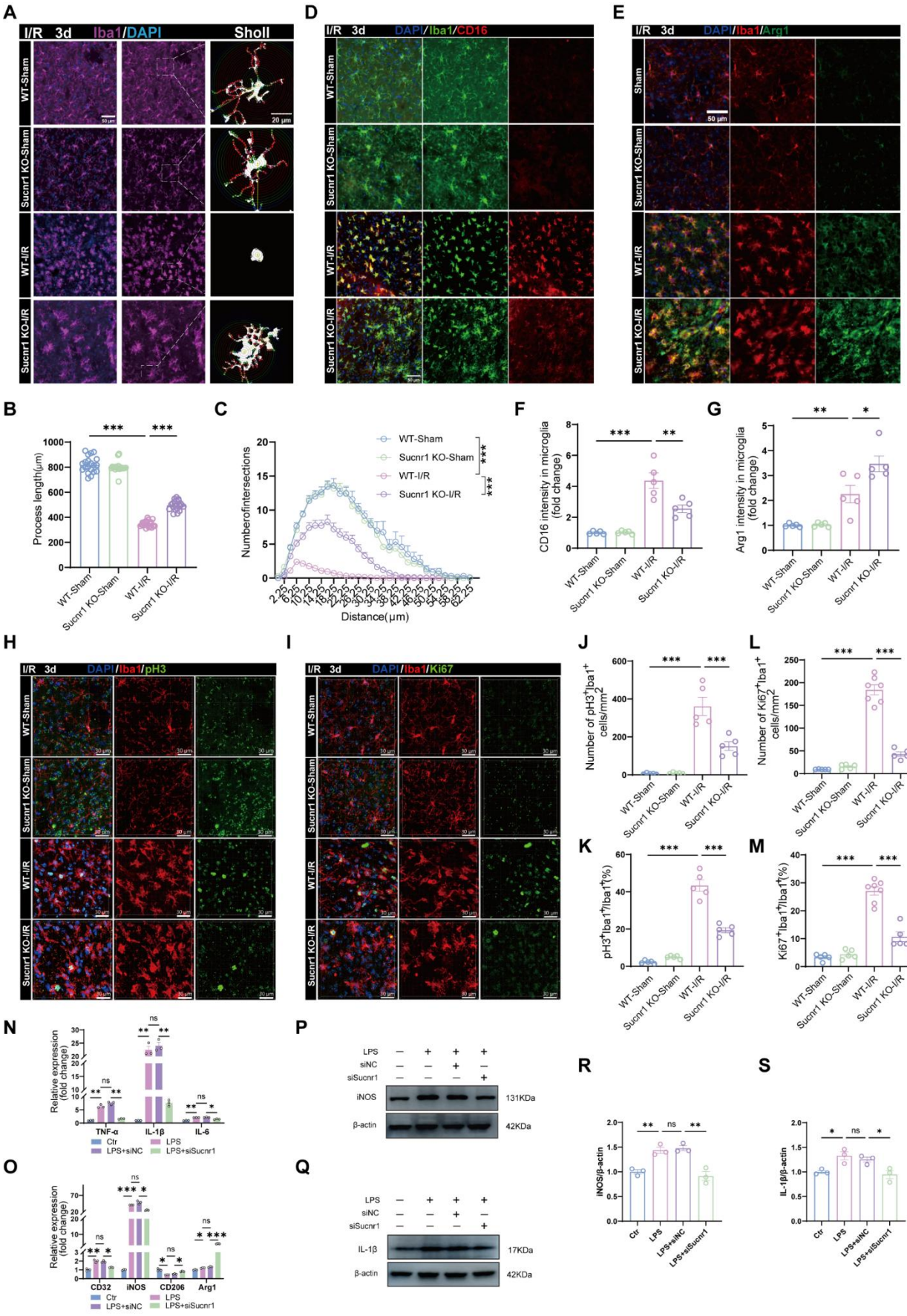


Figure 5. Deletion of Sucnr1 modulates microglial function after acute stroke.

(a) Representative immunofluorescence images showing the expression and morphology of microglia labeled with Iba1 (magenta) in the ipsilateral cortex of each group. Left panels show the overall field (scale bar = 50 μm), and right panels display higher-magnification views used for Sholl analysis (scale bar = 20 μm) to assess microglial morphological complexity.
(b, c) Quantitative analysis of microglial process length (b) and the number of branch intersections at different radial distances from the soma (c) (n = 20–25 cells per group).
(d, e) Immunofluorescence staining illustrating microglial polarization in the acute ischemic stroke model. (d) Colocalization of the microglial marker Iba1 (green) with the M1-like marker CD16 (red); (e) colabeling of Iba1 (red) with the M2 marker Arg1 (green). Scale bar = 50 μm.
(f, g) Quantification of CD16 and Arg1 expression in microglia after Sucnr1 deletion (n = 5–8 per group).
(h, i) Immunofluorescence images showing colocalization of the microglial marker Iba1 with the proliferation markers pH3 (h) and Ki67 (i) in the peri-infarct cortex. Scale bar = 30 μm.
(j, k) Quantification of the number and proportion of $pH3^+$ microglia in the ischemic cortical region of I/R mice (n = 5–8 per group).
(l, m) Quantification of $Ki67^+$ microglial counts and their proportion after I/R injury (n = 5–8 per group).
(n) mRNA expression levels of IL-6, IL-1β, and TNF-α in microglia under different treatments (Ctrl, LPS, LPS + siNC, LPS + siSucnr1) as determined by qPCR.
(o) mRNA expression of pro- and anti-inflammatory polarization markers, including CD32, iNOS, CD206, and Arg1, in microglia (n = 3 per group).
(p, r) Representative immunoblot images and densitometric quantification of iNOS protein levels across groups (n = 3 per group).
(q, s) Representative immunoblots and quantitative analysis of IL-1β protein expression in each treatment group (n = 3 per group).Data are presented as mean ± SEM. Statistical analyses were performed using one-way or two-way ANOVA followed by Tukey's post hoc test. ns = not significant,*$p < 0.05$, **$p < 0.01$, ***$p < 0.001$.

Sucnr1 drives glycolytic reprogramming and inflammatory activation in microglia

Having established that Sucnr1 regulates microglial polarization and inflammatory responses, we next sought to systematically unravel its downstream mechanisms through transcriptomic (Fig.S6a, b)and functional analyses. Using Mfuzz clustering, differentially expressed genes were grouped into six distinct clusters exhibiting dynamic expression patterns over time (Fig.6a,b), among which cluster 5 displayed the most pronounced temporal changes. Pathway enrichment analysis of this cluster revealed significant activation of the glycolytic pathway (Fig.6c), suggesting that Sucnr1 may contribute to microglial metabolic reprogramming toward enhanced glycolysis.

To directly test this hypothesis, microglial metabolic activity was assessed using a Seahorse extracellular flux analyzer. LPS stimulation markedly increased the extracellular acidification rate (ECAR) and overall glycolytic capacity, whereas Sucnr1 knockdown significantly attenuated this LPS-induced glycolytic enhancement (Fig.6d,e). In line with these functional observations, both qPCR and Western blot analyses demonstrated that

silencing Sucnr1 substantially reduced the LPS-induced expression of key glycolytic enzymes, including HK2, LDHA and PKM2, at both the mRNA and protein levels (Fig.6f–h). Consistent with the in vitro findings, Sucnr1 knockout in mice reproduced the key phenotypes observed in cellular models.It attenuated the post-stroke glycolytic surge in microglia, shifted their polarization from a pro-inflammatory M1 state towards an anti-inflammatory M2 state, and consequently reduced the levels of key inflammatory cytokines in the brain tissue(Fig.S8).

Although DSM improves mitochondrial structure and preserves mitochondrial oxidative capacity in primary microglia(Fig.S3), chronic loss of SUCNR1 in BV2 cells appears to disrupt receptor-dependent compensatory signaling required for maintaining mitochondrial function, thereby driving a secondary reliance on glycolysis. Consistently, GO enrichment analysis of differentially expressed genes following Sucnr1 knockdown revealed a significant over-representation of glycolysis-related biological processes (Fig.6i), further reinforcing the tight coupling between SUCNR1 signaling and metabolic remodeling in activated microglia.

In addition to its role in metabolic regulation, clustering analysis also suggested a close association between SUCNR1 signaling and pathways related to microglial phagocytosis and migration(Fig.6i). Furthermore, consistent with this association, genes related to phagocytosis and migration were also suppressed following SUCNR1 knockdown(Fig.S7c,d). We therefore next evaluated the functional consequences of Sucnr1 depletion on these essential microglial behaviors. Flow cytometric analysis revealed that Sucnr1 knockdown significantly decreased the phagocytic capacity of microglia (Fig.6j), consistently,Transwell migration assays revealed a significant alteration in migratory capacity following Sucnr1 silencing (Fig.6k).Together, these data identify Sucnr1 as a key metabolic switch that couples inflammatory activation to glycolytic reprogramming in microglia, while selectively enhancing their phagocytic capacity without altering migratory behavior.

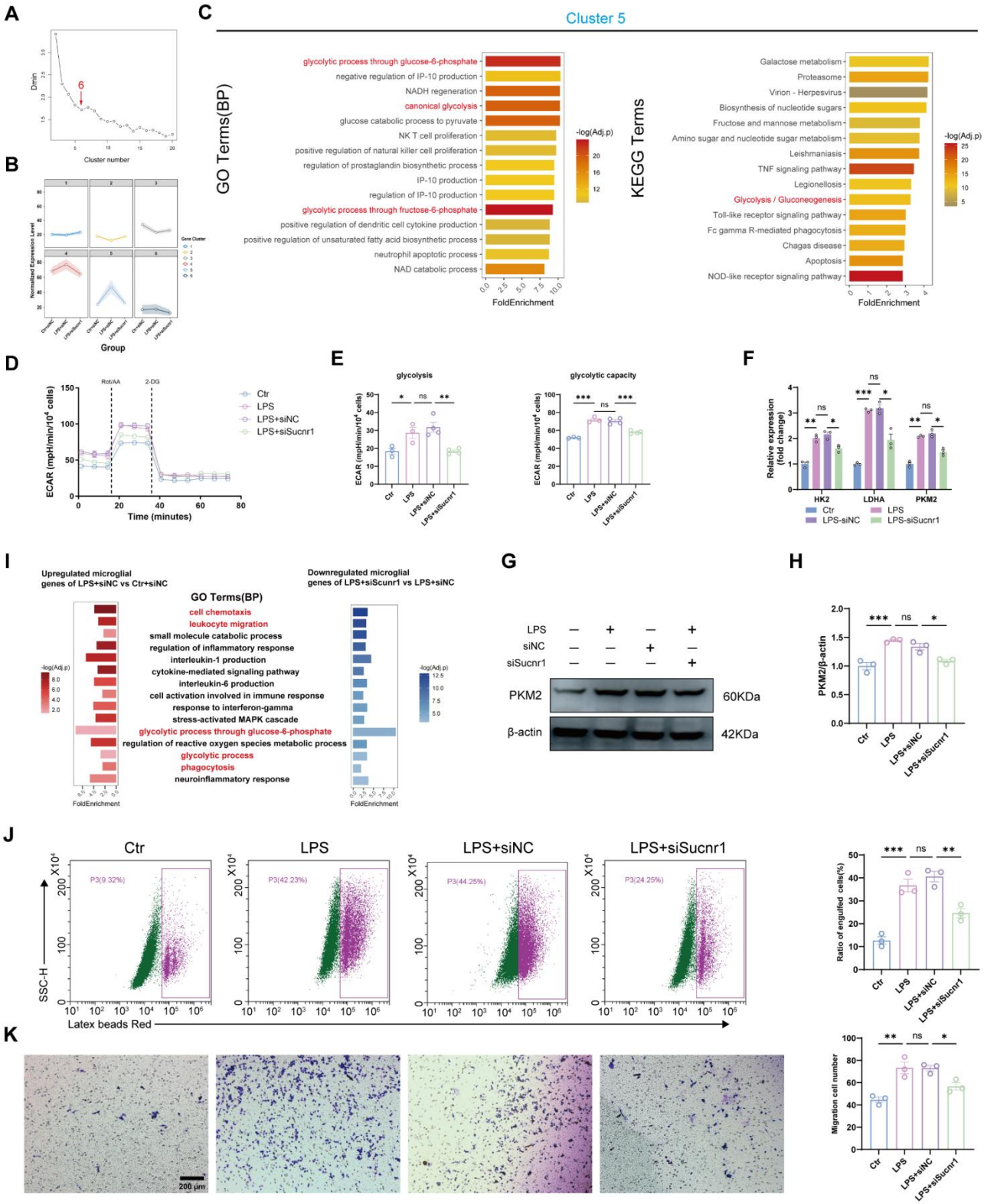


Figure 6. Sucnr1 knockdown reprograms glycolytic pathways and functional states of activated microglia.

(a) Line plot showing the change in Dmin values as the number of clusters increases from 2 to 20. The inflection point, where the Dmin curve begins to plateau, was used to help determine the optimal number of clusters.

(b) Mfuzz clustering analysis identifying six distinct gene expression patterns. Each panel

represents the normalized expression trajectory of genes within a given cluster, with cluster 5 exhibiting the most pronounced dynamic changes.
(c) Bar graph showing Gene Ontology (GO) and pathway enrichment results for genes in cluster 5. The x-axis indicates fold enrichment, the y-axis lists enriched pathways, bar length reflects the degree of enrichment, and color intensity represents statistical significance based on –log(Adj. P).
(d) Seahorse XF analysis of extracellular acidification rate (ECAR) in microglia from different treatment groups (Ctrl, LPS, LPS + siNC, and LPS + siSucnr1), used to evaluate glycolytic activity.
(e) Quantification of basal glycolysis and glycolytic capacity in each group (n = 3–4).
(f) qPCR analysis of mRNA expression levels of key glycolytic enzymes, including HK2, LDHA, and PKM2, in the indicated groups.
(g) Immunoblot analysis of the glycolytic marker protein PKM2 in microglia under different treatments.
(h) Densitometric quantification of PKM2 protein levels in each group.
(i) GO pathway enrichment analysis of commonly differentially expressed genes in the comparisons of LPS + siNC vs Ctrl + siNC and LPS + siSucnr1 vs LPS + siNC; the top 15 significantly enriched pathways are shown.
(j) Flow cytometric assessment of microglial phagocytic capacity, shown as the percentage of microsphere-positive cells in each group (n = 3).
(k) Transwell migration assay showing crystal violet–stained migrated microglia and quantitative analysis of migrated cell numbers (n = 3).Data are presented as mean ± SEM. Statistical analyses were performed using one-way or two-way ANOVA followed by Tukey's post hoc test. ns = not significant, *p < 0.05, **p < 0.01, ***p < 0.001.

HIF-1α mediates Sucnr1-dependent metabolic reprogramming in microglia

Based on our previous findings that Sucnr1 regulates microglial glycolysis, we next sought to identify the upstream signaling axis responsible for this effect. Gene set enrichment analysis revealed that Sucnr1 markedly modulates the HIF-1α signaling pathway and associated immune-response gene sets (Fig.7a), implicating HIF-1α as a potential downstream transcriptional mediator. Subsequent validation at both the protein and transcriptional levels demonstrated that LPS stimulation significantly increased HIF-1α expression in microglia, whereas Sucnr1 knockdown effectively suppressed HIF-1α protein accumulation with minimal impact on its mRNA levels (Fig.7b,c). Consistently, immunofluorescence analysis further confirmed that Sucnr1 silencing markedly reduced the nuclear localization of HIF-1α in microglia (Fig.7d,e).

To determine the functional significance of HIF-1α in Sucnr1-mediated metabolic reprogramming, we performed rescue experiments using the HIF-1α agonist DMOG. Seahorse metabolic analyses showed that DMOG treatment successfully reversed the glycolytic suppression induced by Sucnr1 knockdown, restoring microglial glycolytic capacity (Fig.7f,g). In parallel, Western blot analysis demonstrated that DMOG partially rescued the reduced protein expression of IL-1β, PKM2, and HK2 caused by Sucnr1 knockdown (Fig.7h,i). Functionally, DMOG reversed the impaired phagocytic capacity observed in Sucnr1-deficient microglia (Fig.7j, l), and a similar trend was observed in their

migratory ability (Fig.7k,m).Finally, we performed reverse validation using the HIF-1α–specific inhibitor PX-478. PX-478 treatment effectively suppressed succinate-induced glycolytic activation (Fig.7n,o) and markedly reduced the succinate-mediated upregulation of IL-1β, PKM2, and HK2 at the protein level (Fig. 7p, q). Together, these findings establish that Sucnr1 reprograms microglial glycolysis and inflammatory function by regulating the protein stability and nuclear activity of HIF-1α, thereby defining a coherent Sucnr1/HIF-1α signaling axis.

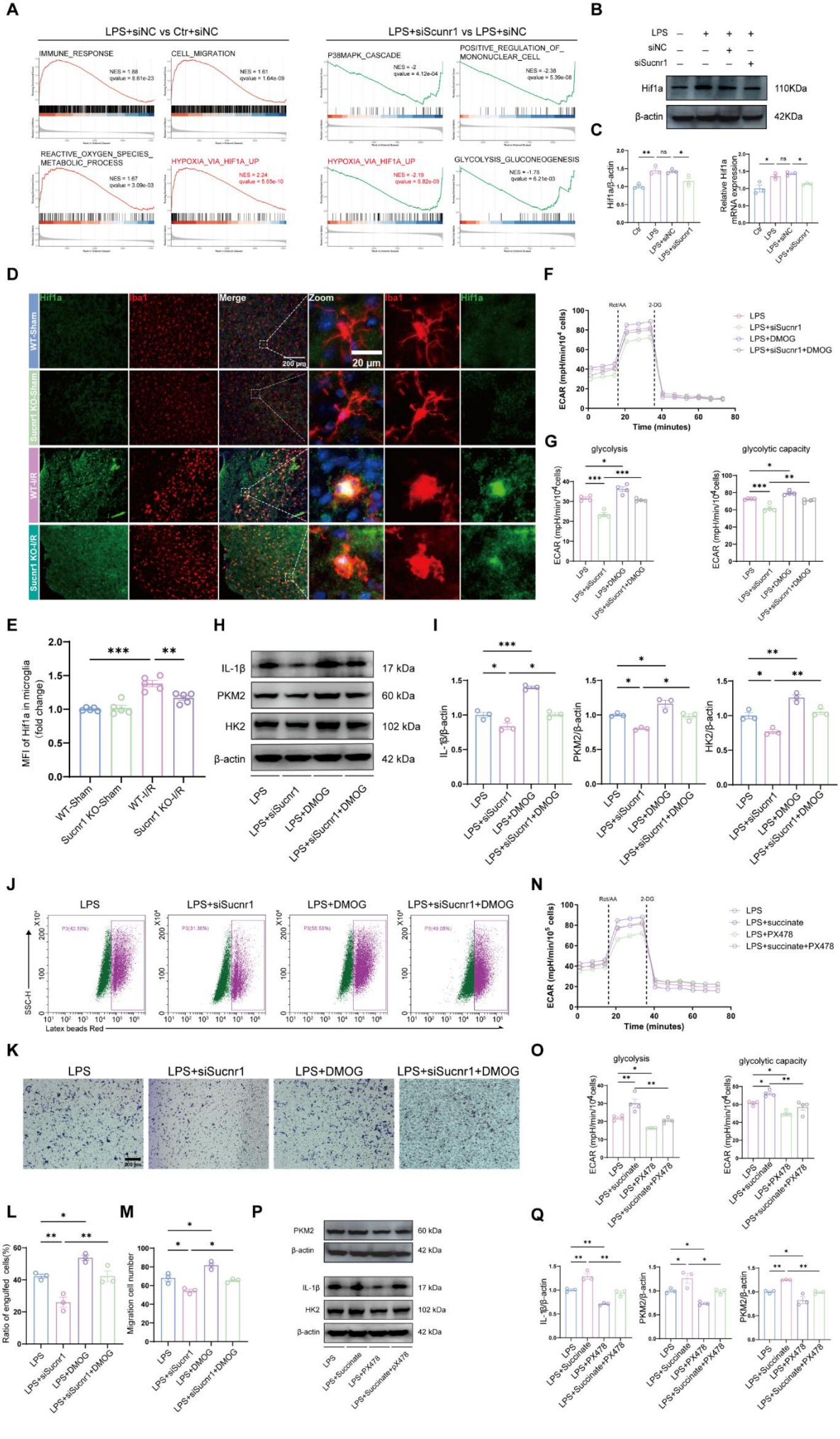

A
LPS+siNC vs Ctr+siNC
IMMUNE_RESPONSE
NES = 1.88
qvalue = 8.61e-23
CELL_MIGRATION
NES = 1.61
qvalue = 1.64e-09
REACTIVE_OXYGEN_SPECIES_METABOLIC_PROCESS
NES = 1.67
qvalue = 3.09e-03
HYPOXIA_VIA_HIF1A_UP
NES = 2.24
qvalue = 5.65e-10
LPS+siScunr1 vs LPS+siNC
P38MAPK_CASCADE
NES = -2
qvalue = 4.12e-04
POSITIVE_REGULATION_OF_MONONUCLEAR_CELL
NES = -2.38
qvalue = 5.39e-08
HYPOXIA_VIA_HIF1A_UP
NES = -2.19
qvalue = 6.82e-09
GLYCOLYSIS_GLUCONEOGENESIS
NES = -1.78
qvalue = 6.21e-03
B
LPS
siNC
siSucnr1
Hif1a
β-actin
110KDa
42KDa
C
Hif1a/β-actin
Relative Hif1a mRNA expression
Ctr
LPS
LPS+siNC
LPS+siSucnr1
D
Hif1a
Iba1
Merge
Zoom
WT-Sham
Sucnr1 KO-Sham
WT-I/R
Sucnr1 KO-I/R
200 μm
20 μm
F
Rot/AA
2-DG
ECAR (mpH/min/10⁴ cells)
Time (minutes)
LPS
LPS+siSucnr1
LPS+DMOG
LPS+siSucnr1+DMOG
G
glycolysis
glycolytic capacity
ECAR (mpH/min/10⁴cells)
E
MFI of Hif1a in microglia (fold change)
WT-Sham
Sucnr1 KO-Sham
WT-I/R
Sucnr1 KO-I/R
H
IL-1β
PKM2
HK2
β-actin
17 kDa
60 kDa
102 kDa
42 kDa
I
IL-1β/β-actin
PKM2/β-actin
HK2/β-actin
J
LPS
LPS+siSucnr1
LPS+DMOG
LPS+siSucnr1+DMOG
P3(42.50%)
P3(31.36%)
P3(56.58%)
P3(49.05%)
SSC-H
Latex beads Red
N
LPS
LPS+succinate
LPS+PX478
LPS+succinate+PX478
K
200 μm
O
L
Ratio of engulfed cells(%)
M
Migration cell number
P
PKM2
β-actin
IL-1β
HK2
60 kDa
42 kDa
17 kDa
102 kDa
Q

Figure 7. Modulation of the Sucnr1/HIF-1α axis reprograms microglial metabolism and function after acute stroke.
(a) Gene set enrichment analysis (GSEA) revealed that Sucnr1 regulates HIF-1α–related signaling pathways, as well as genes involved in immune responses and cell migration.
(b) Representative immunoblot analysis of HIF-1α protein expression in microglia from the Ctrl, LPS, LPS + siNC, and LPS + siSucnr1 groups.
(c) Quantification of HIF-1α protein and mRNA levels in each group (n = 3).
(d) Representative immunofluorescence images showing colocalization of microglia (Iba1, red) and HIF-1α (green) in different groups. Scale bar = 200 μm; magnified images on the right, scale bar = 20 μm.
(e) Quantification of HIF-1α fluorescence intensity in microglia (n = 3 per group).
(f) Seahorse XF analysis showing extracellular acidification rate (ECAR) profiles in microglia treated with LPS, LPS + siSucnr1, LPS + DMOG, and LPS + siSucnr1 + DMOG.
(g) Quantification of basal glycolysis and glycolytic capacity in each group (n = 3).
(h) Western blot analysis of IL-1β, PKM2, and HK2 protein expression in microglia under the indicated conditions.
(i) Densitometric quantification of IL-1β, PKM2, and HK2 protein levels (n = 3).
(j, l) Flow cytometric analysis of microglial phagocytic capacity, expressed as the percentage of microsphere-positive cells, and quantification across groups (n = 3).
(k, m) Transwell migration assay showing crystal violet-stained migrated microglia and quantitative analysis of migrated cell numbers (n = 3).
(n) Seahorse XF analysis of ECAR in microglia treated with LPS, LPS + succinate, LPS + PX-478, and LPS + succinate + PX-478.
(o) Quantification of glycolytic parameters, including basal glycolysis and glycolytic capacity, in each group (n = 3).
(p) Western blot analysis of IL-1β, PKM2, and HK2 protein expression under the indicated treatments.
(q) Quantification of IL-1β, PKM2, and HK2 protein expression by densitometry (n = 3).Data are presented as mean ± SEM. Statistical analyses were performed using one-way or two-way ANOVA followed by Tukey's post hoc test.*$p < 0.05$, **$p < 0.01$, ***$p < 0.001$.

Development of an RGD-functionalized nanoplatform for targeted delivery of DSM to the ischemic brain

Building on the critical pathogenic role of the succinate/Sucnr1/HIF-1α signaling axis in ischemic stroke and the well-defined neuroprotective effect of the succinate dehydrogenase inhibitor malonate (DSM), we sought to develop a nanodrug delivery system capable of targeting DSM specifically to the ischemic brain region, thereby overcoming the limitations of systemic administration.We successfully synthesized mesoporous silica nanoparticles loaded with DSM. Scanning electron microscopy revealed that the nanoparticles exhibited a uniform and well-defined spherical morphology (Fig.8a). Dynamic light scattering analysis showed a narrow hydrodynamic size distribution centered at approximately 200 nm (Fig.8b), while zeta potential measurements further confirmed their surface charge characteristics (Fig.8c). Transmission electron microscopy clearly

demonstrated the typical mesoporous structure of the nanoparticles (Fig.8d). Energy-dispersive X-ray spectroscopy (Fig.8e) and elemental mapping (Fig. 8f) confirmed the successful incorporation and homogeneous distribution of key elements, including Si, O, N, and Na, within the nanoparticles.To verify surface functionalization and drug loading, Fourier-transform infrared spectroscopy was performed. The spectra confirmed successful amine functionalization on the nanoparticle surface (Fig.8g) as well as the efficient conjugation of the RGD targeting peptide and encapsulation of DSM (Fig.8h). In addition, UV–visible absorption spectroscopy combined with a BCA protein assay further validated the successful attachment of RGD peptides on the nanoparticle surface (Fig.8i).

Following material characterization, we evaluated the biocompatibility and targeting capability of the nanoplatform. CCK-8 assays demonstrated that both blank nanoparticles (M) and RGD-modified DSM-loaded nanoparticles (MNDR) exhibited no detectable cytotoxicity toward BV2 microglial cells, even at high concentrations (Fig. 8j), indicating excellent biocompatibility.We then examined cellular uptake using confocal microscopy to visualize Cy5-labeled nanoparticles in BV2 cells. Compared with the non-RGD-modified MND group, the MNDR group displayed markedly stronger intracellular red fluorescence, indicating that RGD modification significantly enhanced microglial internalization of the nanoparticles (Fig. 8k, m). Importantly, this enhanced uptake was substantially attenuated by competitive inhibition with free RGD peptides, providing strong evidence for the specificity of the RGD-mediated active targeting mechanism (Fig. 8k, m).

Finally, the in vivo targeting capability of the nanoparticles was validated in a mouse cerebral ischemia–reperfusion model. Ex vivo fluorescence imaging of brain tissues revealed that, compared with the free Cy5 group, empty nanoparticles (Cy5@MN), and non-RGD-modified drug-loaded nanoparticles (Cy5@MND), the RGD-functionalized drug-loaded nanoparticles (Cy5@MNDR) exhibited the strongest fluorescence signal within the ischemic hemisphere (Fig. 8l, n). These results clearly demonstrate that the engineered MNDR nanosystem efficiently and specifically accumulates in the ischemic brain region.

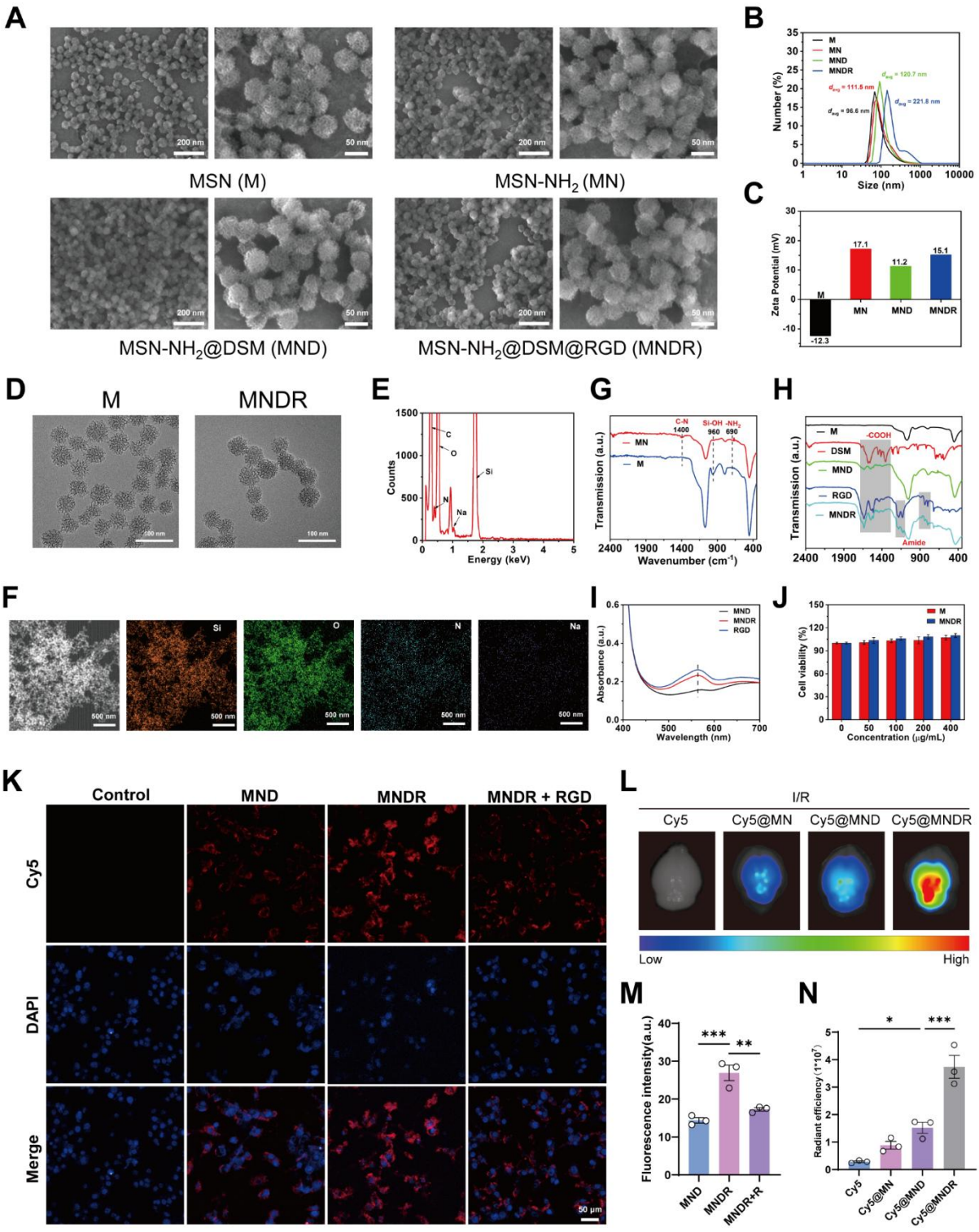


Figure 8.Characterization and targeting validation of DSM-loaded mesoporous nanoparticles.

(a) Representative scanning electron microscopy (SEM) images of the synthesized nanoparticles. Scale bars = 200 nm (left) and 50 nm (right).

(b) Hydrodynamic size distribution of the nanoparticles measured by dynamic light scattering (DLS).

(c) Zeta potential analysis of the nanoparticles.

(d) Transmission electron microscopy (TEM) images of M and MNDR nanoparticles. Scale bar = 100 nm.
(e) Energy-dispersive X-ray spectroscopy (EDS) analysis of the MNDR nanoparticles.
(f) Elemental mapping of MNDR nanoparticles. The upper-left panel shows the corresponding bright-field image, while the remaining four pseudocolor images indicate the spatial distribution of Si (orange), O (green), N (blue), and Na (purple). Scale bar = 500 nm.
(g) Fourier transform infrared (FTIR) spectra of nanoparticles before and after amine functionalization.
(h) FTIR spectra of M, MND, MNDR, DSM, and RGD, confirming successful loading and surface modification.
(i) UV–Vis absorption spectra obtained from the bicinchoninic acid (BCA) protein assay.
(j) Cell viability of BV2 microglial cells treated with different concentrations of M and MNDR nanoparticles, evaluated by CCK-8 assay.
(k, m) Confocal laser scanning microscopy (CLSM) images and quantification of mean red fluorescence intensity in cells incubated with Cy5-labeled nanoparticles. Cy5-labeled nanoparticles appear red, and nuclei are counterstained with DAPI (blue). Three groups were analyzed: MND (DSM-loaded), MNDR (DSM-loaded + RGD-modified), and MNDR + RGD competition group (cells pretreated with free RGD for 1 h before MNDR exposure). Nanoparticle concentration = 400 μg mL^{-1}; incubation time = 2 h. Scale bar = 50 μm (n = 3).
(l, n) Ex vivo fluorescence imaging of mouse brains at 22 h after injection in the acute ischemia–reperfusion model, along with quantification of mean fluorescence intensity. Four groups were included: free dye (Cy5), unloaded nanoparticles (Cy5@MN), DSM-loaded nanoparticles (Cy5@MND), and RGD-modified DSM-loaded nanoparticles (Cy5@MNDR). The color scale ranges from blue (low intensity) to red (high intensity). Data are presented as mean ± SEM. Statistical analyses were performed using one-way or two-way ANOVA followed by Tukey's post hoc test.*$p < 0.05$, **$p < 0.01$, ***$p < 0.001$.

Targeted MNDR therapy attenuates post-stroke neuroinflammation and brain injury by reprogramming microglial metabolism

Having successfully constructed and validated the targeted MNDR nanodelivery system, we next evaluated its therapeutic efficacy in regulating post-stroke microglial metabolism and attenuating brain injury both in vitro and in vivo.First, Seahorse metabolic analysis revealed that, compared with LPS stimulation alone, treatment with MNDR nanoparticles markedly suppressed microglial glycolysis, as evidenced by significant reductions in extracellular acidification rate (ECAR), basal glycolytic activity, and glycolytic capacity (Fig. 9a–c). Consistently, ELISA and qPCR analyses showed that MNDR treatment significantly decreased the secretion and gene expression of pro-inflammatory cytokines, including IL-6, TNF-α, and IL-1β, while simultaneously promoting the production of the anti-inflammatory cytokine IL-10 (Fig. 9d, e). These findings indicate that MNDR effectively reverses microglial metabolic reprogramming and inflammatory activation.In the in vivo ischemia–reperfusion model, the therapeutic potential of MNDR was further confirmed.

Compared with the untreated I/R group and the free DSM-treated group, MNDR administration significantly promoted microglial polarization toward the M2 anti-

inflammatory phenotype while suppressing the M1 pro-inflammatory phenotype (Fig. 9f–i). TTC staining demonstrated a marked reduction in infarct volume following MNDR treatment (Fig. 9j), accompanied by significantly decreased levels of pro-inflammatory cytokines in brain tissue (Fig. 9k).Functionally, open field testing and modified neurological severity score assessments revealed that mice treated with MNDR exhibited markedly improved motor performance and accelerated neurological recovery after stroke (Fig. 9l, m), with therapeutic efficacy superior to that achieved by free DSM administration.Together, these results demonstrate that DSM-loaded, RGD-targeted nanoparticles effectively suppress neuroinflammation by modulating microglial glycolytic metabolism, reduce ischemic brain injury, and significantly promote functional recovery, thereby offering a promising translational therapeutic strategy for ischemic stroke.

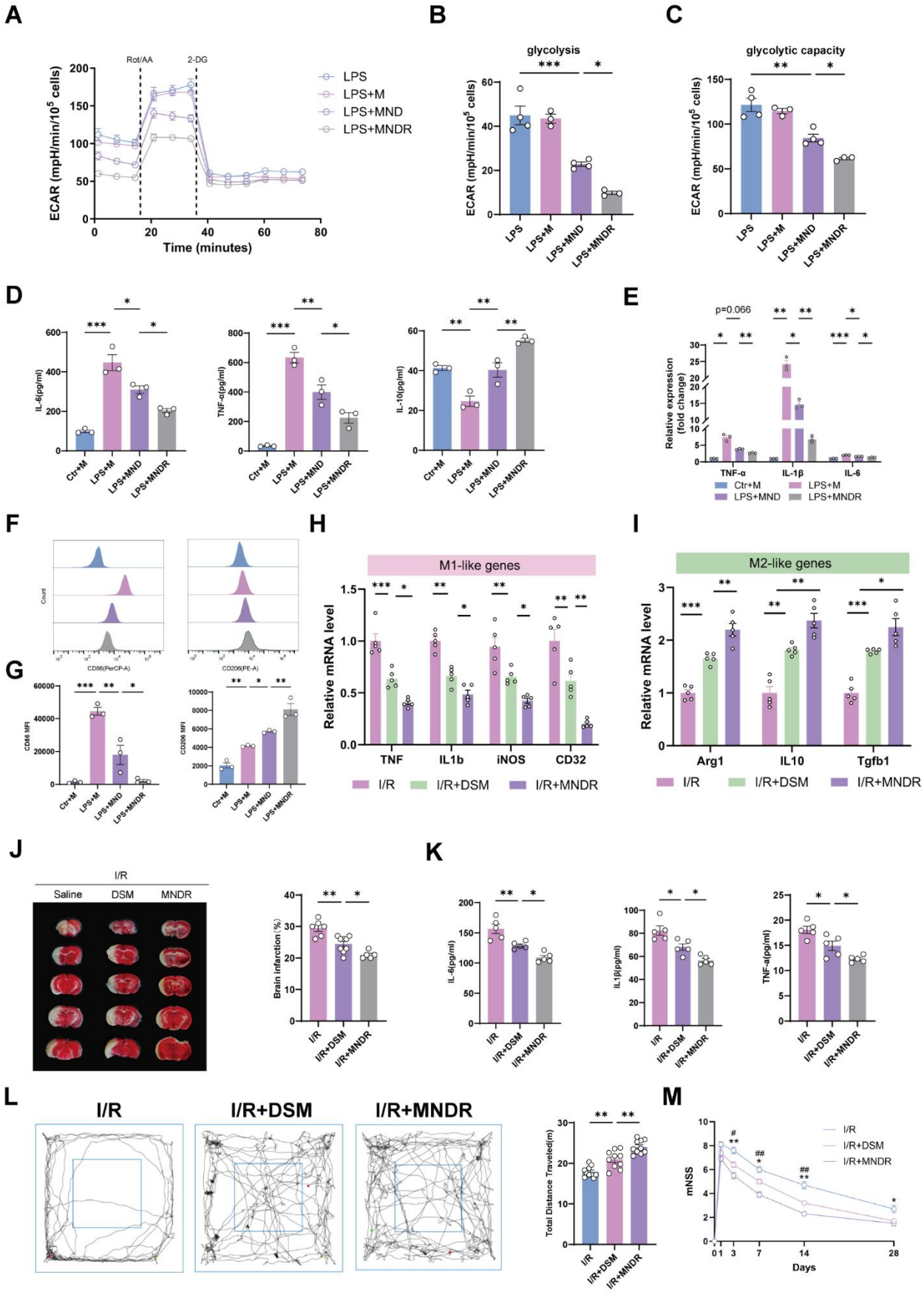


Figure 9. DSM-loaded mesoporous nanoparticles attenuate microglial glycolysis

and reduce brain injury after acute stroke.

(a) Seahorse XF–recorded extracellular acidification rate (ECAR) profiles of microglia in the four groups: LPS, LPS + M, LPS + MND, and LPS + MNDR.

(b) Basal glycolysis, calculated as the difference between the ECAR peak and baseline levels (n = 3).

(c) Glycolytic capacity in each group (n = 3).

(d) ELISA quantification of IL-6, TNF-α, and IL-10 levels in culture supernatants (n = 3).

(e) mRNA expression levels of TNF-α, IL-1β, and IL-6 in microglia.

(f, g) Flow cytometric analysis of microglial polarization status.

(h, i) mRNA expression of M1 and M2 polarization markers in the brains of post-stroke mice (n = 5–6 per group).

(j) Representative TTC staining images at 24 h after I/R showing infarct areas in the I/R, I/R + DSM, and I/R + MNDR groups, along with quantitative analysis of infarct volume (n = 5–9).

(k) ELISA assessment of inflammatory cytokines (IL-6, IL-1β, and TNF-α) in brain tissue from each group (n = 5).

(l) Open-field test showing representative locomotor trajectories and quantification of total distance traveled in the I/R, I/R + DSM, and I/R + MNDR groups (n = 12).

(m) Dynamic changes in the modified neurological severity score (mNSS) from pre-surgery (baseline) to 28 days post-stroke (n = 10–12 per group).

Data are presented as mean ± SEM. Statistical analyses were performed using one-way or two-way ANOVA followed by Tukey's post hoc test. ns = not significant, *$p < 0.05$, **$p < 0.01$, ***$p < 0.001$.

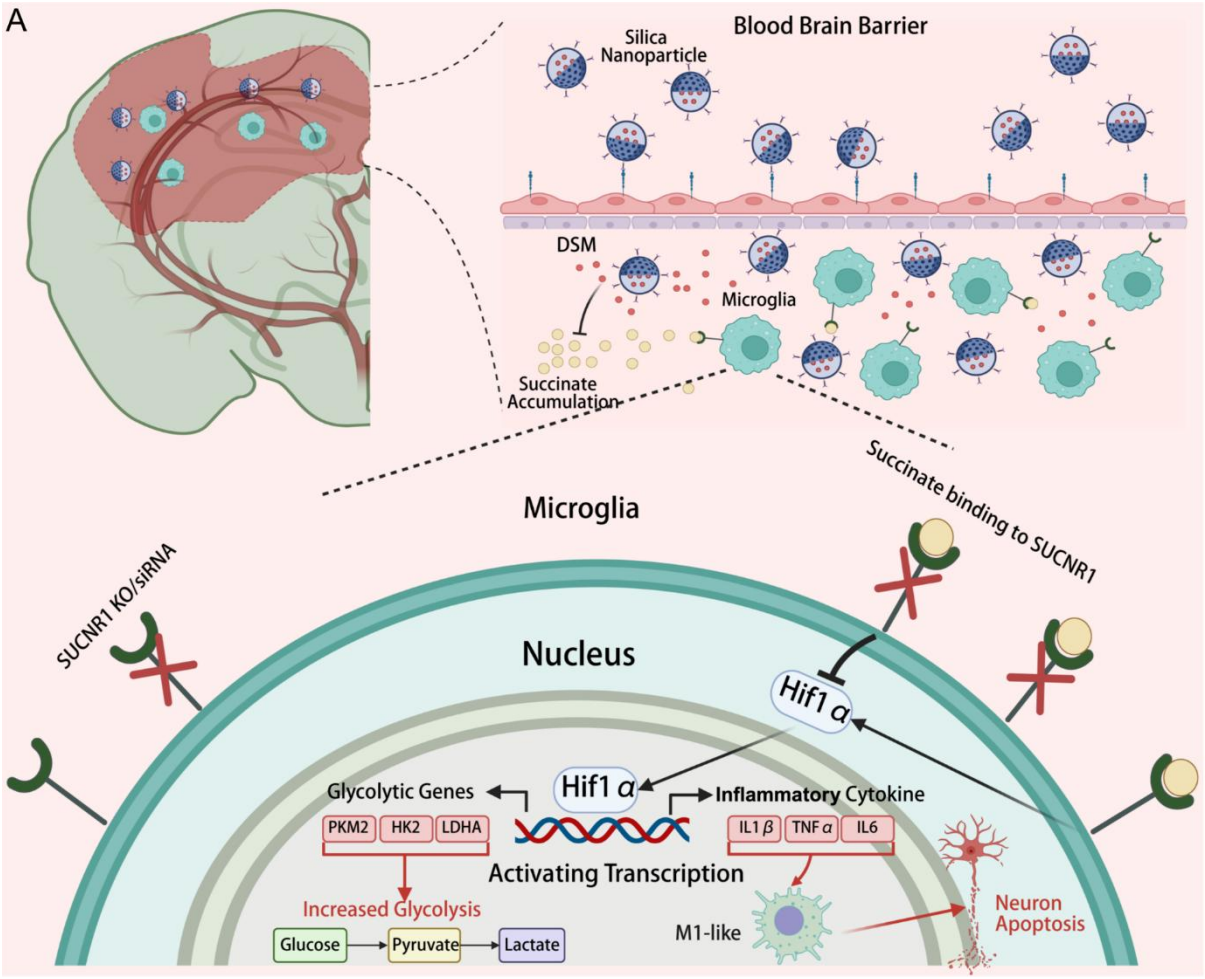


Figure 10. Metabolic Reprogramming and Inflammatory Responses in Microglia After Cerebral Ischemia-Reperfusion Injury.

(a) Following targeted delivery to ischemic brain regions, DSM is released from RGD-functionalized nanoparticles and binds to Sucnr1 on microglia. Sucnr1 activation promotes glycolytic reprogramming through the upregulation of HK2, LDHA, and PKM2, which stabilizes HIF-1α and enhances the transcription of pro-inflammatory cytokines, including IL-1β, TNF-α, and IL-6. This signaling cascade drives M1 microglial polarization, neuroinflammation, and neuronal apoptosis. In contrast, Sucnr1 knockout or Sucnr1-targeting siRNA effectively blocks this pathway, thereby suppressing glycolytic reprogramming, HIF-1α-mediated inflammatory signaling, M1 polarization, and TUNEL-positive neuronal apoptosis(by BioRender).

4.Discussion

In the present study, we systematically demonstrate that succinate accumulation represents a conserved and pathogenic metabolic hallmark of ischemic stroke and functions as an active driver of neuroinflammation rather than a passive byproduct of metabolic failure. By integrating human brain tissue data, an independent clinical cohort, and mechanistic experiments in both in vivo and in vitro models, we identify a succinate–SUCNR1–HIF-1α signaling axis in microglia that couples ischemia-induced metabolic dysregulation to inflammatory amplification and secondary neuronal injury(Fig.10). Below, we discuss how succinate accumulation acquires pathological significance after ischemic

stroke, how SUCNR1 enables microglia to sense and transduce this metabolic signal, and how downstream HIF-1α activation and glycolytic reprogramming may provide a mechanistic basis for targeted therapeutic intervention.

Metabolic disruption is a hallmark of ischemic stroke, yet the roles of individual metabolites in shaping disease progression remain incompletely defined. Our metabolomic analyses reveal that succinate accumulation is a robust and reproducible response to ischemia–reperfusion, consistently observed in human ischemic brain tissue, experimental mouse models, and the circulation of stroke patients[35,36]. Importantly, elevated succinate levels correlated strongly with infarct severity and unfavorable clinical outcomes, and multivariable regression analysis identified succinate as an independent prognostic risk factor[37,38]. These findings extend prior observations of ischemia-induced succinate accumulation and establish its clinical relevance in human stroke. Functional manipulation of succinate availability provided direct evidence for its pathogenic role. Exogenous succinate supplementation exacerbated infarct volume, worsened neurological deficits, and amplified neuroinflammation[38], pharmacological inhibition with malonate conferred marked neuroprotection[35]. Notably, although inhibition of succinate dehydrogenase would be expected to increase succinate under classical oxidative TCA cycle conditions, ischemic succinate accumulation occurs through a distinct metabolic context in which SDH can operate in reverse. In this setting, fumarate overflow derived from purine nucleotide breakdown and partial reversal of the malate–aspartate shuttle drives succinate production during ischemia. Thus, inhibition of SDH within the ischemic phase may limit reverse SDH-dependent succinate generation and reduce the pathological net accumulation of succinate, rather than simply blocking succinate oxidation[13]. This interpretation is consistent with our observation that DSM reduced ischemia-induced succinate accumulation and attenuated downstream inflammatory injury. Collectively, these results support the concept that succinate is not merely a metabolic marker of ischemic stress but a causal mediator that aggravates ischemic brain injury.

Having established succinate as a pathogenic mediator rather than merely a marker of ischemic stress[20,39,40], it becomes important to define how this metabolite is sensed within the ischemic brain. We identify SUCNR1 as the principal receptor through which extracellular succinate drives microglial inflammatory activation after ischemic stroke. Although SUCNR1 has been studied in peripheral immune cells and metabolic tissues[13,20,41], its role in the central nervous system—particularly in microglia under ischemic conditions—has remained largely unexplored. We demonstrate that SUCNR1 expression is selectively upregulated in microglia within the ischemic hemisphere, with minimal changes observed in neurons or astrocytes, highlighting a cell-type–specific response to ischemic metabolic stress. Genetic deletion or knockdown of Sucnr1 markedly attenuated neurological deficits, reduced neuronal apoptosis, and suppressed microglial proliferation and inflammatory activation after stroke[13,42]. Although the M1/M2 framework oversimplifies the dynamic and heterogeneous nature of microglial responses after stroke, it remains a useful operational classification for describing the inflammatory and inflammation-resolving features observed in this study. Within this framework, these protective effects were accompanied by a shift in microglial phenotype toward a more ramified, homeostatic-like morphology, reduced M1-like inflammatory activation, and

enhanced M2-like inflammation-resolving features[43,44]. This expands the role of succinate from an intracellular mitochondrial intermediate to an extracellular immunometabolic signal capable of instructing microglial behavior in the ischemic brain.

Beyond its established role in inflammatory signaling, our findings reveal that SUCNR1 sustains post-ischemic microglial inflammation by modulating the metabolic state required for prolonged immune activation. Given that persistent activation of myeloid cells is tightly linked to metabolic rewiring, especially a shift toward glycolysis, we examined whether SUCNR1 signaling regulates microglial glycolytic responses after ischemic injury. Transcriptomic profiling and pathway enrichment analyses revealed that SUCNR1 signaling strongly influences glycolysis-related gene networks[45–47]. Functional metabolic assays confirmed that Sucnr1 knockdown or deletion significantly suppressed glycolytic flux and glycolytic capacity in activated microglia, accompanied by downregulation of key glycolytic enzymes [48]. Together, these transcriptomic and functional metabolic data support a model in which SUCNR1 signaling reinforces microglial inflammatory activation by driving glycolytic reprogramming after ischemic injury. Such metabolic reprogramming is increasingly recognized as a prerequisite for sustained inflammatory activation in immune cells [49]. By linking extracellular succinate sensing to intracellular metabolic remodeling, SUCNR1 may therefore provide a mechanistic bridge between ischemia-driven metabolic stress and microglial inflammatory effector functions [47,50]. These observations suggest that SUCNR1-dependent metabolic remodeling requires a transcriptional program capable of coordinating glycolysis and inflammatory activation.

To further define how SUCNR1 activation is translated into glycolytic and inflammatory transcriptional programs, we focused on HIF-1α, a central regulator of hypoxia-responsive metabolism and inflammatory gene expression. Our findings identify HIF-1α as a key downstream effector of SUCNR1 signaling in microglia, linking extracellular metabolic stress to redox-sensitive transcriptional reprogramming under ischemic conditions[40,47]. Although succinate has been shown to stabilize HIF-1α through inhibition of prolyl hydroxylases in other contexts, our data demonstrate that SUCNR1 signaling critically regulates HIF-1α protein accumulation and nuclear localization in microglia without substantially altering its transcription. Rescue experiments using the HIF-1α agonist DMOG and inhibition with PX-478 further establish that HIF-1α activity is necessary and sufficient to mediate SUCNR1-dependent glycolytic reprogramming and inflammatory gene expression[17,51].

Importantly, the impact of SUCNR1/HIF-1α signaling was not limited to cytokine production or metabolic remodeling. Microglial responses after stroke encompass not only inflammatory mediator production but also functional behaviors such as debris clearance and lesion-directed migration. Our observation that Sucnr1 knockdown reduced both phagocytic capacity and migratory responses suggests that SUCNR1 participates in broader injury-responsive microglial programs, rather than solely amplifying inflammatory gene expression [43,52]. This finding highlights the complexity of targeting SUCNR1 therapeutically: effective intervention should restrain maladaptive inflammatory metabolism without completely abolishing microglial functions required for tissue surveillance and repair.

These findings provide a mechanistic rationale for targeting the succinate–SUCNR1–HIF-1α axis in ischemic stroke. Because systemic modulation of succinate metabolism may affect multiple tissues, efficient and lesion-directed delivery is critical[13,53]. However, effective delivery of metabolic inhibitors to the ischemic brain remains a major challenge[54,55]. To address this, we developed an RGD-modified mesoporous nanoparticle system for targeted delivery of the succinate dehydrogenase inhibitor DSM. By limiting succinate accumulation at the metabolic origin of this pathway, DSM may reduce extracellular succinate availability, attenuate SUCNR1 activation, and suppress downstream HIF-1α-dependent glycolytic and inflammatory reprogramming in microglia. This nanoplatform exhibited favorable biocompatibility, selective accumulation in ischemic brain regions, and superior therapeutic efficacy compared with free DSM administration. By suppressing microglial glycolysis and inflammatory activation, the targeted nanotherapy significantly reduced infarct volume and improved long-term functional recovery, underscoring the translational potential of targeting immunometabolic pathways in ischemic stroke[56]. Thus, spatially restricted targeting of succinate-driven immunometabolic signaling may represent a feasible strategy to mitigate post-ischemic neuroinflammation while minimizing systemic metabolic interference.

Conclusions, limitations, and future directions

In summary, our study defines succinate as a key metabolic driver of post-ischemic neuroinflammation and identifies SUCNR1 as a central microglial receptor that couples extracellular metabolic stress signals to intracellular inflammatory and metabolic reprogramming via HIF-1α. By elucidating this succinate–SUCNR1–HIF-1α axis, our work provides a mechanistic link between ischemia-driven metabolic imbalance and redox-associated inflammatory amplification in the post-stroke brain.

Several limitations should be acknowledged. First, although SUCNR1 was preferentially upregulated in microglia after ischemic stroke and Sucnr1 deletion or knockdown attenuated microglial inflammatory and metabolic activation, the use of global Sucnr1 knockout mice precludes definitive attribution of the neuroprotective effects exclusively to microglial SUCNR1. Potential contributions from other neurovascular unit cells, including endothelial cells and pericytes, cannot be excluded. Moreover, constitutive Sucnr1 deletion may have systemic consequences because SUCNR1 is also expressed in peripheral metabolically active tissues, particularly white adipose tissue. Sucnr1 has been reported to regulate adipose mass, glucose homeostasis, adipocyte-derived leptin dynamics, adipose tissue macrophage infiltration, and osteoclastogenesis[24,57–59]. Therefore, potential changes in body weight, leptin secretion, systemic energy metabolism, muscle function, exercise adaptability, postnatal growth, neuromuscular innervation, or skeletal development could indirectly influence ischemic injury and behavioral recovery. Although no gross abnormalities were observed during routine animal handling, these systemic parameters were not systematically examined. Thus, future studies using inducible microglia-specific Sucnr1 conditional knockout mice or cell-type-specific rescue strategies are required to define the cell-autonomous role of microglial SUCNR1 in stroke pathology. Second, although HIF-1α was identified as a key downstream mediator, the proximal signaling events linking SUCNR1 activation to HIF-1α stabilization under ischemic redox stress remain to be defined. Finally, larger multicenter cohorts are needed to validate

circulating succinate as a prognostic biomarker. Future studies should clarify the cell-type-specific roles of SUCNR1, resolve its downstream redox-sensitive signaling nodes, and optimize metabolic-targeted therapies in combination with reperfusion-based treatments.

Data availability

The metabolic data of human and mouse warm ischemia models are adapted from Mottahedin A et al., Redox Biology, 2023. The raw sequencing data generated in this study have been deposited in the Figshare(10.6084/m9.figshare.32660016
).

Ethics Approval and Consent to Participate

The studies involving human participants were reviewed and approved by the Institutional Ethics Committee of Minhang Hospital, Fudan University (Approval Number: 2021-008-01K), and informed consent was obtained from all participants.

Competing Interests

The authors declare no competing interests.

Author Contributions

Z.L., Z.Z., and K.Y. contributed equally to this work, participating in study design,performing the majority of experiments and writing. Z.Z. and X.M.assisted with in vitro experiments and data analysis. H.N.and M.C.contributed to in vivo experiments. Z.Z.and R.J.helped with immunoblotting and qPCR analysis. Y.W. and J.Z. conceived and supervised the study, and were responsible for funding acquisition.Y.W. and J.Z.critically revised the manuscript. All authors reviewed and approved the final version.

Acknowledgements

Not applicable.

Funding

This work was supported by the STI 2030-Major Projects (2022ZD0204704, 2021ZD0201704), the National Natural Science Foundation of China (grant nos. 82173646 and 82373703), and the Public Health Discipline Construction Project of Shanghai Minhang District Health Commission (MGWXK2023-04).

Reference

1. Chamorro Á, Dirnagl U, Urra X, Planas AM. Neuroprotection in acute stroke: targeting excitotoxicity, oxidative and nitrosative stress, and inflammation. The Lancet Neurology. 2016;15:869–81. https://doi.org/10.1016/S1474-4422(16)00114-9

2. Iadecola C, Buckwalter MS, Anrather J. Immune responses to stroke: mechanisms, modulation, and therapeutic potential. Journal of Clinical Investigation. 2020;130:2777–88. https://doi.org/10.1172/JCI135530

3. Jayaraj RL, Azimullah S, Beiram R, Jalal FY, Rosenberg GA. Neuroinflammation: friend and foe for ischemic stroke. J Neuroinflammation. 2019;16:142. https://doi.org/10.1186/s12974-019-1516-2

4. Qin C, Zhou L-Q, Ma X-T, Hu Z-W, Yang S, Chen M, et al. Dual Functions of Microglia in Ischemic Stroke. Neurosci Bull. 2019;35:921–33. https://doi.org/10.1007/s12264-019-00388-3

5. Li Q, Barres BA. Microglia and macrophages in brain homeostasis and disease. Nat Rev Immunol. 2018;18:225–42. https://doi.org/10.1038/nri.2017.125

6. Xu S, Lu J, Shao A, Zhang JH, Zhang J. Glial cells: role of the immune response in ischemic stroke. Front Immunol. 2020;11:294. https://doi.org/10.3389/fimmu.2020.00294

7. Jin R, Yang G, Li G. Inflammatory mechanisms in ischemic stroke: role of inflammatory cells. Journal of Leukocyte Biology. 2010;87:779–89. https://doi.org/10.1189/jlb.1109766

8. Shi K, Tian D-C, Li Z-G, Ducruet AF, Lawton MT, Shi F-D. Global brain inflammation in stroke. Lancet Neurol. 2019;18:1058–66. https://doi.org/10.1016/S1474-4422(19)30078-X

9. Lambertsen KL, Finsen B, Clausen BH. Post-stroke inflammation—target or tool for therapy? Acta Neuropathol. 2019;137:693–714. https://doi.org/10.1007/s00401-018-1930-z

10. O'Neill LAJ, Kishton RJ, Rathmell J. A guide to immunometabolism for immunologists. Nat Rev Immunol. 2016;16:553–65. https://doi.org/10.1038/nri.2016.70

11. Buck MD, Sowell RT, Kaech SM, Pearce EL. Metabolic Instruction of Immunity. Cell. 2017;169:570–86. https://doi.org/10.1016/j.cell.2017.04.004

12. Loftus RM, Finlay DK. Immunometabolism: Cellular Metabolism Turns Immune Regulator. Journal of Biological Chemistry. 2016;291:1–10. https://doi.org/10.1074/jbc.R115.693903

13. Chouchani ET, Pell VR, Gaude E, al et. Ischaemic accumulation of succinate controls reperfusion injury through mitochondrial ROS. Nature. 2014;515:431–5. https://doi.org/10.1038/nature13909

14. Mills EL, Kelly B, O'Neill LAJ. Mitochondria are the powerhouses of immunity. Nat Immunol. 2017;18:488–98. https://doi.org/10.1038/ni.3704

15. Tretter L, Patocs A, Chinopoulos C. Succinate, an intermediate in metabolism, signal transduction, ROS, hypoxia, and tumorigenesis. Biochim Biophys Acta. 2016;1857:1086–101. https://doi.org/10.1016/j.bbabio.2016.03.012

16. Selak MA, Armour SM, MacKenzie ED, Boulahbel H, Watson DG, Mansfield KD, et al. Succinate links TCA cycle dysfunction to oncogenesis by inhibiting HIF-alpha prolyl hydroxylase. Cancer Cell. 2005;7:77–85. https://doi.org/10.1016/j.ccr.2004.11.022

17. Tannahill GM, Curtis AM, Adamik J, al et. Succinate is an inflammatory signal that induces IL-1β through HIF-1α. Nature. 2013;496:238–42. https://doi.org/10.1038/nature11986

18. Rubic T, Lametschwandtner G, Jost S, Hinteregger S, Kund J, Carballido-Perrig N, et al. Triggering the succinate receptor GPR91 on dendritic cells enhances immunity. Nat Immunol. 2008;9:1261–9. https://doi.org/10.1038/ni.1657

19. Peruzzotti-Jametti L, Donegá M, Giusto E, Mallucci G, Marchetti B, Pluchino S. The role of the immune system in central nervous system plasticity after acute injury. Neuroscience. 2014;283:210–21. https://doi.org/10.1016/j.neuroscience.2014.04.036

20. Littlewood-Evans A, Sarret S, Apfel V, Loesle P, Dawson J, Zhang J, et al. GPR91 senses extracellular succinate released from inflammatory macrophages and exacerbates rheumatoid arthritis. J Exp Med. 2016;213:1655–62. https://doi.org/10.1084/jem.20160061

21. He W, Miao FJ-P, Lin DC-H, Schwandner RT, Wang Z, Gao J, et al. Citric acid cycle intermediates as ligands for orphan G-protein-coupled receptors. Nature. 2004;429:188–93. https://doi.org/10.1038/nature02488

22. Bozic M, Grünler J, Jensen V, al et. GPR91: expanding the frontiers of Krebs cycle intermediates. Cell Commun Signal. 2016;14:76. https://doi.org/10.1186/s12964-016-0126-1

23. Michaely E, Shara M. White dwarf - main sequence star collisions from wide triples in the field. Monthly Notices of the Royal Astronomical Society. 2021;502:4540–6. https://doi.org/10.1093/mnras/stab339

24. van Diepen JA, Robben JH, Hooiveld GJ, Carmone C, Alsady M, Boutens L, et al. SUCNR1-mediated chemotaxis of macrophages aggravates obesity-induced inflammation and diabetes. Diabetologia. 2017;60:1304–13. https://doi.org/10.1007/s00125-017-4261-z

25. Keiran N, Ceperuelo-Mallafré V, Calvo E, Hernández-Alvarez MI, Ejarque M, Núñez-Roa C, et al. SUCNR1 controls an anti-inflammatory program in macrophages to regulate the metabolic response to obesity. Nat Immunol. 2019;20:581–92. https://doi.org/10.1038/s41590-019-0372-7

26. Sadagopan N, Li W, Roberds SL, Major T, Preston GM, Yu Y, et al. Circulating succinate is elevated in rodent models of hypertension and metabolic disease. Am J Hypertens. 2007;20:1209–15. https://doi.org/10.1016/j.amjhyper.2007.05.010

27. Macias-Ceja DC, Ortiz-Masiá D, Salvador P, Gisbert-Ferrándiz L, Hernández C, Hausmann M, et al. Succinate receptor mediates intestinal inflammation and fibrosis. Mucosal Immunol. 2019;12:178–87. https://doi.org/10.1038/s41385-018-0087-3

28. Li J, Yang Y-L, Li L-Z, Zhang L, Liu Q, Liu K, et al. Succinate accumulation impairs cardiac pyruvate dehydrogenase activity through GRP91-dependent and independent signaling pathways: Therapeutic effects of ginsenoside Rb1. Biochimica et Biophysica Acta (BBA) - Molecular Basis of Disease. 2017;1863:2835–47. https://doi.org/10.1016/j.bbadis.2017.07.017

29. Hamel D, Sanchez M, Duhamel F, Roy O, Honoré J-C, Noueihed B, et al. G-protein-coupled receptor 91 and succinate are key contributors in neonatal postcerebral hypoxia-ischemia recovery. Arterioscler Thromb Vasc Biol. 2014;34:285–93. https://doi.org/10.1161/ATVBAHA.113.302131

30. Mu X, Zhao T, Xu C, Shi W, Geng B, Shen J, et al. Oncometabolite succinate promotes angiogenesis by upregulating VEGF expression through GPR91-mediated STAT3 and ERK activation. Oncotarget. 2017;8:13174–85. https://doi.org/10.18632/oncotarget.14485

31. Zhang Z, Huang S, Wang Y, Jiang Z, Liu Z, Wang C, et al. Flipping the Switch: MeCP2-Mediated Lactylation Rewires Microglial Metabolism and Inflammation via the HK2/mTOR Axis in Poststroke Neuroinflammation. Adv Sci (Weinh). 2025;e13400. https://doi.org/10.1002/advs.202513400

32. Zhang Z, Jin P, Guo Z, Tu Z, Yang H, Hu M, et al. Integrated Analysis of Chromatin and Transcriptomic Profiling Identifies PU.1 as a Core Regulatory Factor in Microglial Activation Induced by Chronic Cerebral Hypoperfusion. Mol Neurobiol. 2024;61:2569–89. https://doi.org/10.1007/s12035-023-03734-9

33. Wang Y, Liu Z, Li L, Zhang Z, Zhang K, Chu M, et al. Anti-ferroptosis exosomes engineered for targeting M2 microglia to improve neurological function in ischemic stroke. J Nanobiotechnology. 2024;22:291. https://doi.org/10.1186/s12951-024-02560-y

34. Garcia JH, Wagner S, Liu KF, Hu XJ. Neurological deficit and extent of neuronal necrosis attributable to middle cerebral artery occlusion in rats. Statistical validation. Stroke. 1995;26:627–34; discussion 635. https://doi.org/10.1161/01.str.26.4.627

35. Mottahedin A, Prag HA, Dannhorn A, Mair R, Schmidt C, Yang M, et al. Targeting succinate metabolism to decrease brain injury upon mechanical thrombectomy treatment of ischemic stroke. Redox Biol. 2023;59:102600. https://doi.org/10.1016/j.redox.2023.102600

36. Mao M, Cao X, Liang Y, Li Q, Chen S, Zhou L, et al. Neuroprotection of rhubarb extract against cerebral ischaemia-reperfusion injury via the gut-brain axis pathway. Phytomedicine. 2024;126:155254. https://doi.org/10.1016/j.phymed.2023.155254

37. Li Y, Zhang Y-N, Zhang P-L, Li Y-C, Zhang L, Yang H, et al. Inhibition of citrate transport reduces HIF-1α/GABA-T-mediated succinate accumulation in macrophages: The role of astragaloside IV in ischemic stroke. Phytomedicine. 2025;139:156449. https://doi.org/10.1016/j.phymed.2025.156449

38. Huang LY, Ma JY, Song JX. Ischemic Accumulation of Succinate Induces Cdc42 Succinylation. Neural Regeneration Research. 2022;18:1040–5. https://doi.org/10.4103/1673-5374.355761

39. Huang H, Li G, He Y, Chen J, Yan J, Zhang Q, et al. Cellular succinate metabolism and signaling in inflammation: implications for therapeutic intervention. Front Immunol. 2024;15:1404441. https://doi.org/10.3389/fimmu.2024.1404441

40. Peruzzotti-Jametti L, Bernstock JD, Vicario N, Costa ASH, Kwok CK, Leonardi T, et al. Macrophage-Derived Extracellular Succinate Licenses Neural Stem Cells to Suppress Chronic Neuroinflammation. Cell Stem Cell. 2018;22:355-368.e13. https://doi.org/10.1016/j.stem.2018.01.020

41. Mills EL, O'Neill LA. Succinate: a metabolic signal in inflammation. Trends Cell Biol. 2014;24:313–20. https://doi.org/10.1016/j.tcb.2013.11.008

42. Trauelsen M, Hiron TK, Lin D, Petersen JE, Breton B, Husted AS, et al. Extracellular succinate hyperpolarizes M2 macrophages through SUCNR1/GPR91-mediated Gq signaling. Cell Reports. 2021;35:109246. https://doi.org/10.1016/j.celrep.2021.109246

43. Wu KK. Extracellular Succinate: A Physiological Messenger and a Pathological Trigger. Int J Mol Sci. 2023;24:11165. https://doi.org/10.3390/ijms241311165

44. Zhang W, Lang R. Succinate metabolism: a promising therapeutic target for inflammation, ischemia/reperfusion injury and cancer. Front Cell Dev Biol. 2023;11:1266973. https://doi.org/10.3389/fcell.2023.1266973

45. Sanchez M, Hamel D, Bajon E, Duhamel F, Bhosle VK, Zhu T, et al. The Succinate Receptor SUCNR1 Resides at the Endoplasmic Reticulum and Relocates to the Plasma Membrane in Hypoxic Conditions. Cells. 2022;11:2185. https://doi.org/10.3390/cells11142185

46. Xu J, Zheng Y, Zhao Y, Zhang Y, Li H, Zhang A, et al. Succinate/IL-1β Signaling Axis Promotes the Inflammatory Progression of Endothelial and Exacerbates Atherosclerosis. Front Immunol. 2022;13:817572. https://doi.org/10.3389/fimmu.2022.817572

47. Diaconescu IB, Dumitru AV, Tataru CP, Toader C, Șerban M, Covache-Busuioc R-A, et al. From Electron Imbalance to Network Collapse: Decoding the Redox Code of Ischemic Stroke for Biomarker-Guided Precision Neuroprotection. Int J Mol Sci. 2025;26:10835. https://doi.org/10.3390/ijms262210835

48. Murphy MP, O'Neill LAJ. Krebs Cycle Reimagined: The Emerging Roles of Succinate and Itaconate as Signal Transducers. Cell. 2018;174:780–4. https://doi.org/10.1016/j.cell.2018.07.030

49. Suresh MV, Aktay S, Yalamanchili G, Solanki S, Sathyarajan DT, Arnipalli MS, et al. Role of succinate in airway epithelial cell regulation following traumatic lung injury. JCI Insight. 2023;8:e166860. https://doi.org/10.1172/jci.insight.166860

50. Fernández-Veledo S, Ceperuelo-Mallafré V, Vendrell J. Rethinking succinate: an unexpected hormone-like metabolite in energy homeostasis. Trends Endocrinol Metab. 2021;32:680–92. https://doi.org/10.1016/j.tem.2021.06.003

51. Semenza GL. Hypoxia-Inducible Factors in Physiology and Medicine. Cell. 2012;148:399–408. https://doi.org/10.1016/j.cell.2012.01.021

52. Nimmerjahn A, Kirchhoff F, Helmchen F. Resting Microglial Cells Are Highly Dynamic Surveillants of Brain Parenchyma in Vivo. Science. 2005;308:1314–8. https://doi.org/10.1126/science.1110647

53. Hauser AS, Attwood MM, Rask-Andersen M, Schiöth HB, Gloriam DE. Trends in GPCR drug discovery: new agents, targets and indications. Nat Rev Drug Discov. 2017;16:829–42. https://doi.org/10.1038/nrd.2017.178

54. Deng L, Zhang F, Wu Y, Luo J, Mao X, Long L, et al. RGD-Modified Nanocarrier-Mediated Targeted Delivery of HIF-1α-AA Plasmid DNA to Cerebrovascular Endothelial Cells for Ischemic Stroke Treatment. ACS Biomater Sci Eng. 2019;5:6254–64. https://doi.org/10.1021/acsbiomaterials.9b01362

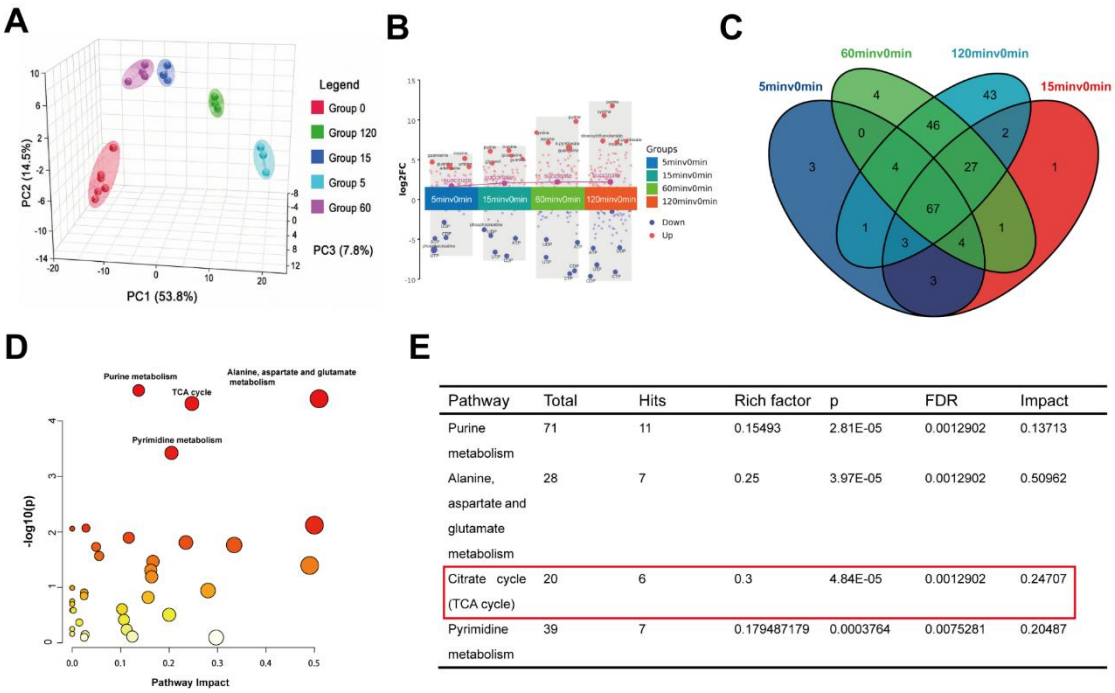
55. Bonnard T, Gauberti M, Martinez De Lizarrondo S, Campos F, Vivien D. Recent Advances in Nanomedicine for Ischemic and Hemorrhagic Stroke. Stroke. 2019;50:1318–24. https://doi.org/10.1161/STROKEAHA.118.022744

56. Lv W, Liu Y, Li S, Lv L, Lu H, Xin H. Advances of nano drug delivery system for the theranostics of ischemic stroke. J Nanobiotechnology. 2022;20:248. https://doi.org/10.1186/s12951-022-01450-5

57. McCreath KJ, Espada S, Gálvez BG, Benito M, de Molina A, Sepúlveda P, et al. Targeted disruption of the SUCNR1 metabolic receptor leads to dichotomous effects on obesity. Diabetes. 2015;64:1154–67. https://doi.org/10.2337/db14-0346

58. Villanueva-Carmona T, Cedó L, Madeira A, Ceperuelo-Mallafré V, Rodríguez-Peña M-M, Núñez-Roa C, et al. SUCNR1 signaling in adipocytes controls energy metabolism by modulating circadian clock and leptin expression. Cell Metab. 2023;35:601-619.e10. https://doi.org/10.1016/j.cmet.2023.03.004

59. Guo Y, Xie C, Li X, Yang J, Yu T, Zhang R, et al. Succinate and its G-protein-coupled receptor stimulates osteoclastogenesis. Nat Commun. 2017;8:15621. https://doi.org/10.1038/ncomms15621



Pathway	Total	Hits	Rich factor	p	FDR	Impact
Purine metabolism	71	11	0.15493	2.81E-05	0.0012902	0.13713
Alanine, aspartate and glutamate metabolism	28	7	0.25	3.97E-05	0.0012902	0.50962
Citrate cycle (TCA cycle)	20	6	0.3	4.84E-05	0.0012902	0.24707
Pyrimidine metabolism	39	7	0.179487179	0.0003764	0.0075281	0.20487

Figure S1. Common differentially expressed metabolites are enriched in the TCA cycle at different time points in the warm ischemia mouse model.

(a) Principal component analysis (PCA) showing the distribution of brain metabolites at different time points after warm ischemia in mice. Data are adapted from Mottahedin A et al., *Redox Biology*, 2023.

(b) Volcano plots illustrating upregulated and downregulated metabolites at each time point.

(c) Venn diagram displaying the overlap of differentially expressed metabolites across pairwise group comparisons.

(d, e) Pathway enrichment analyses indicating significant enrichment of the tricarboxylic acid (TCA) cycle among the differentially expressed metabolites.

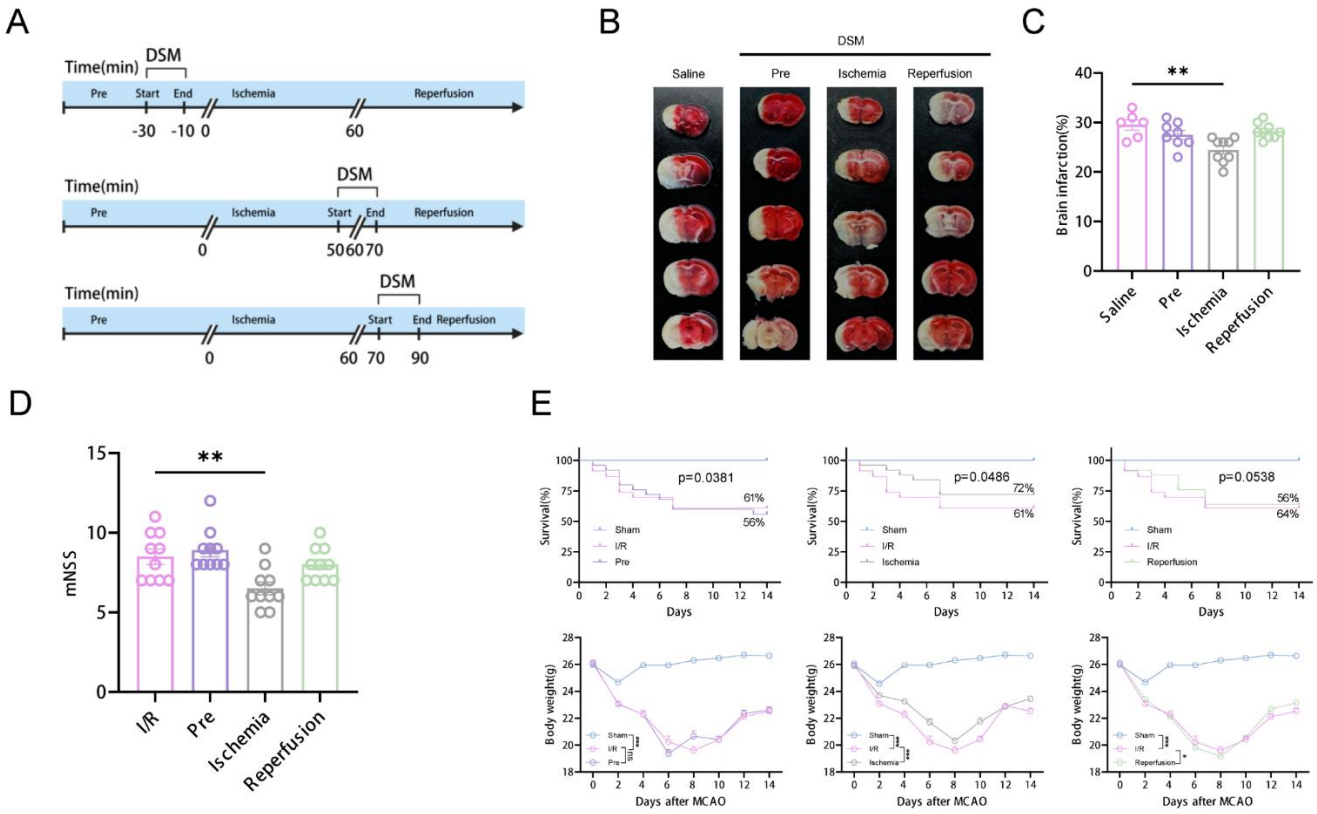


Figure S2. Administration of DSM during the ischemic phase confers optimal therapeutic effects in ischemic stroke.

(a) Schematic illustration of DSM administration at different stages: pre-ischemia, during ischemia, and after reperfusion (created with BioRender).

(b) Representative TTC-stained images showing the effects of DSM treatment at different time points on acute ischemia–reperfusion brain injury.

(c) Quantitative analysis of infarct volume measured by TTC staining at different administration time points (n = 6–9).

(d) Modified neurological severity score (mNSS) assessed on day 7 after acute ischemia–reperfusion.

(e) Survival rate and body weight changes of mice treated with DSM during the ischemic phase in the acute I/R model (n = 12–25).

Data are presented as mean ± SEM. Statistical analyses were performed using one-way or two-way ANOVA followed by Tukey's post hoc test. ns = not significant, *p < 0.05, **p < 0.01, ***p* < 0.001.

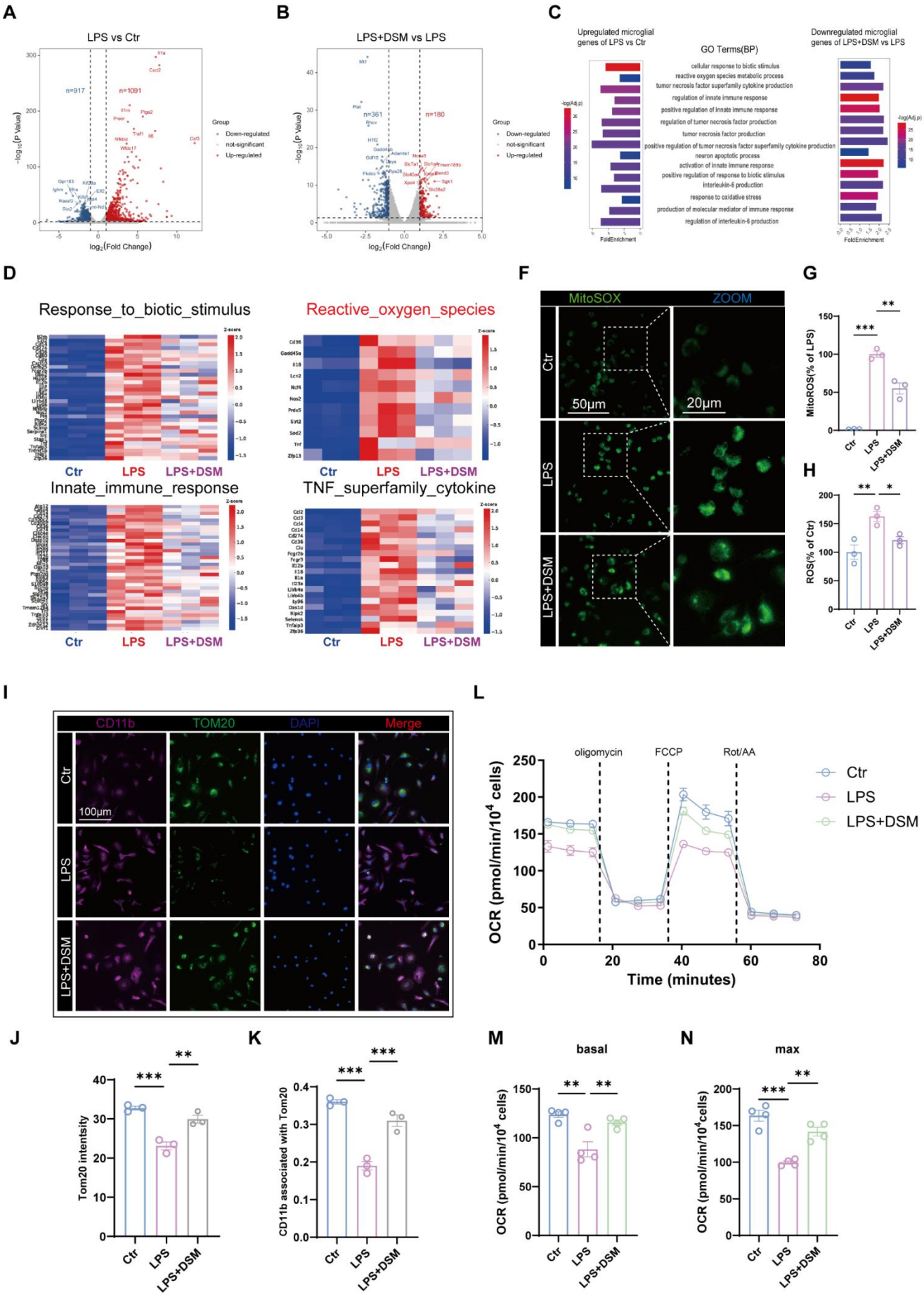

A
LPS vs Ctr
n=917
n=1091
Group
Down-regulated
not-significant
Up-regulated
log2(Fold Change)
B
LPS+DSM vs LPS
n=361
n=180
C
Upregulated microglial genes of LPS vs Ctr
GO Terms(BP)
Downregulated microglial genes of LPS+DSM vs LPS
cellular response to biotic stimulus
reactive oxygen species metabolic process
tumor necrosis factor superfamily cytokine production
regulation of innate immune response
positive regulation of innate immune response
regulation of tumor necrosis factor production
tumor necrosis factor production
positive regulation of tumor necrosis factor superfamily cytokine production
neuron apoptotic process
activation of innate immune response
positive regulation of response to biotic stimulus
interleukin-6 production
response to oxidative stress
production of molecular mediator of immune response
regulation of interleukin-6 production
FoldEnrichment
D
Response_to_biotic_stimulus
Reactive_oxygen_species
Innate_immune_response
TNF_superfamily_cytokine
Ctr
LPS
LPS+DSM
F
MitoSOX
ZOOM
50μm
20μm
G
MitoROS(% of LPS)
H
ROS(% of Ctr)
I
CD11b
TOM20
DAPI
Merge
100μm
L
oligomycin
FCCP
Rot/AA
OCR (pmol/min/10^4 cells)
Time (minutes)
J
Tom20 intentsity
K
CD11b associated with Tom20
M
basal
N
max

Figure S3. DSM regulates transcriptomic pathway enrichment and attenuates mitochondrial oxidative stress in microglia.

(a, b) Differential gene expression analysis presented as volcano plots, with significantly altered genes defined by |logFC| > 1 and adjusted $P < 0.05$ (n = 3).

(c) Pathway enrichment analysis showing that genes upregulated in the LPS vs Ctrl comparison and downregulated in the LPS + DSM vs LPS comparison were significantly enriched in multiple shared Gene Ontology (GO) biological processes, including cellular response to biological stimuli, reactive oxygen species (ROS) metabolic process, interleukin-6 (IL-6) production, inflammatory cytokine generation, regulation and activation of immune responses, and neuronal apoptosis.

(d) Heatmap illustrating expression patterns of genes involved in key biological processes, including cellular response to biological stimuli, ROS metabolic process, innate immune response, and tumor necrosis factor (TNF) superfamily cytokine production, across different treatment groups.

(e) MitoSOX fluorescence staining showing mitochondrial superoxide levels in primary microglia under different treatments. Scale bars = 50 μm (left) and 20 μm (right).

(f, g) Quantitative analysis of mitochondrial and intracellular ROS levels in primary microglia following DSM treatment.

(h) Immunofluorescence images showing the expression of the mitochondrial outer membrane marker TOM20 in primary microglia. Scale bar = 100 μm.

(i, j) Quantification of TOM20 fluorescence intensity and the proportion of TOM20-positive cells after DSM intervention.

(k) Seahorse XF mitochondrial stress test measuring the oxygen consumption rate (OCR) in primary microglia under control (Ctrl), LPS, and LPS + DSM conditions.

(l) Quantification of basal respiration (basal OCR).

(m) Quantification of maximal respiratory capacity (maximal OCR).

Data are presented as mean ± SEM. Statistical analyses were performed using one-way ANOVA followed by Tukey's post hoc test.*p < 0.05, **p < 0.01, **p < 0.001.

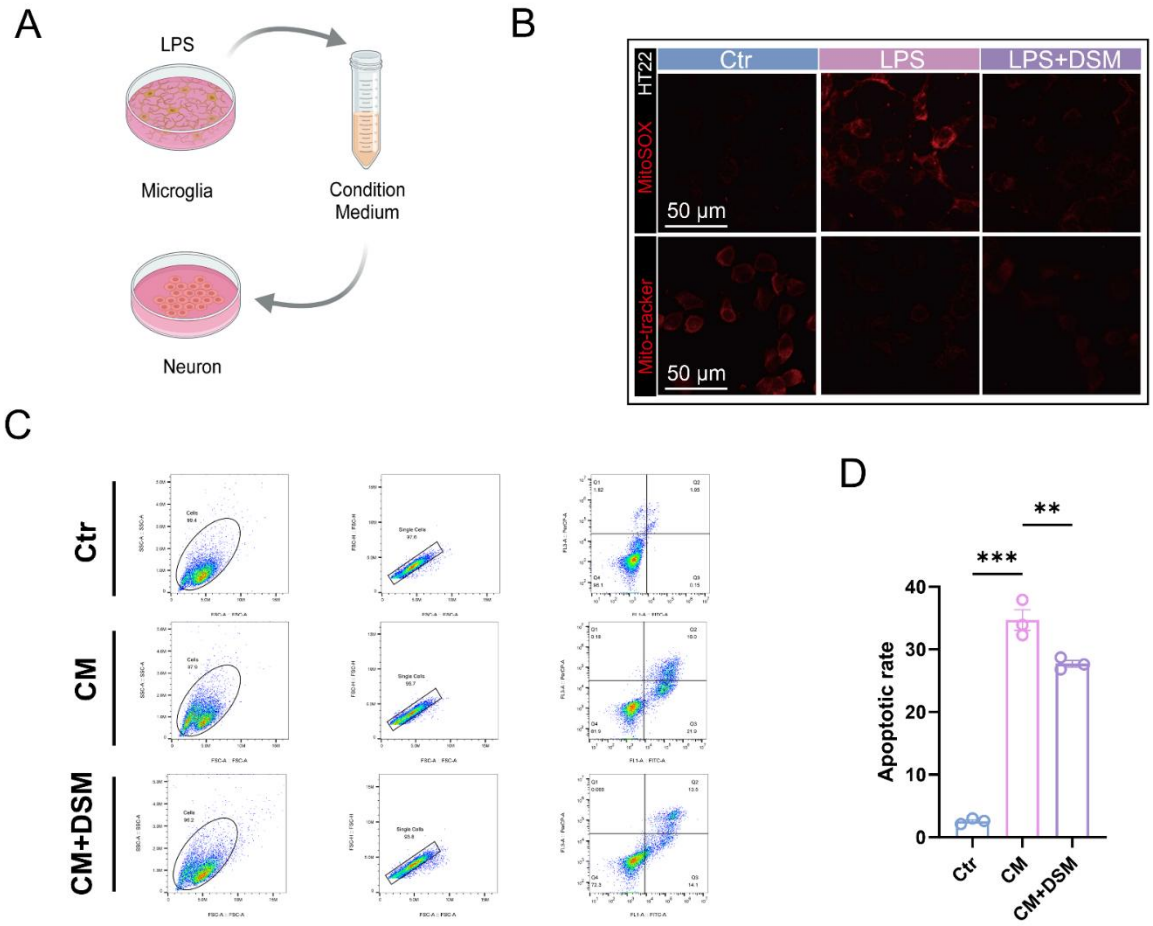


Figure S4. DSM ameliorates neuronal mitochondrial dysfunction and apoptosis under a microglia-mediated inflammatory microenvironment.

(a) Schematic illustration of the experimental workflow (created with BioRender). Primary microglia were stimulated with LPS, and the conditioned medium (CM) was collected and applied to HT22 mouse hippocampal neuronal cultures. Three experimental groups were established: Control (Ctr, culture medium from untreated microglia), CM (conditioned medium from LPS-stimulated microglia), and CM + DSM (conditioned medium from microglia treated with both LPS and DSM).

(b) Representative fluorescence microscopy images showing changes in mitochondrial reactive oxygen species (ROS) levels and mitochondrial morphology in neurons, as detected by MitoSOX and MitoTracker staining. Scale bar = 50 μm.

(c) Flow cytometric dot plots illustrating the distribution of neuronal cell populations in each group.

(d) Quantitative analysis of neuronal apoptosis following DSM treatment.

Data are presented as mean ± SEM. Statistical analyses were performed using one-way ANOVA followed by Tukey's post hoc test. $^{**}p < 0.01$, $^{***}p < 0.001$.

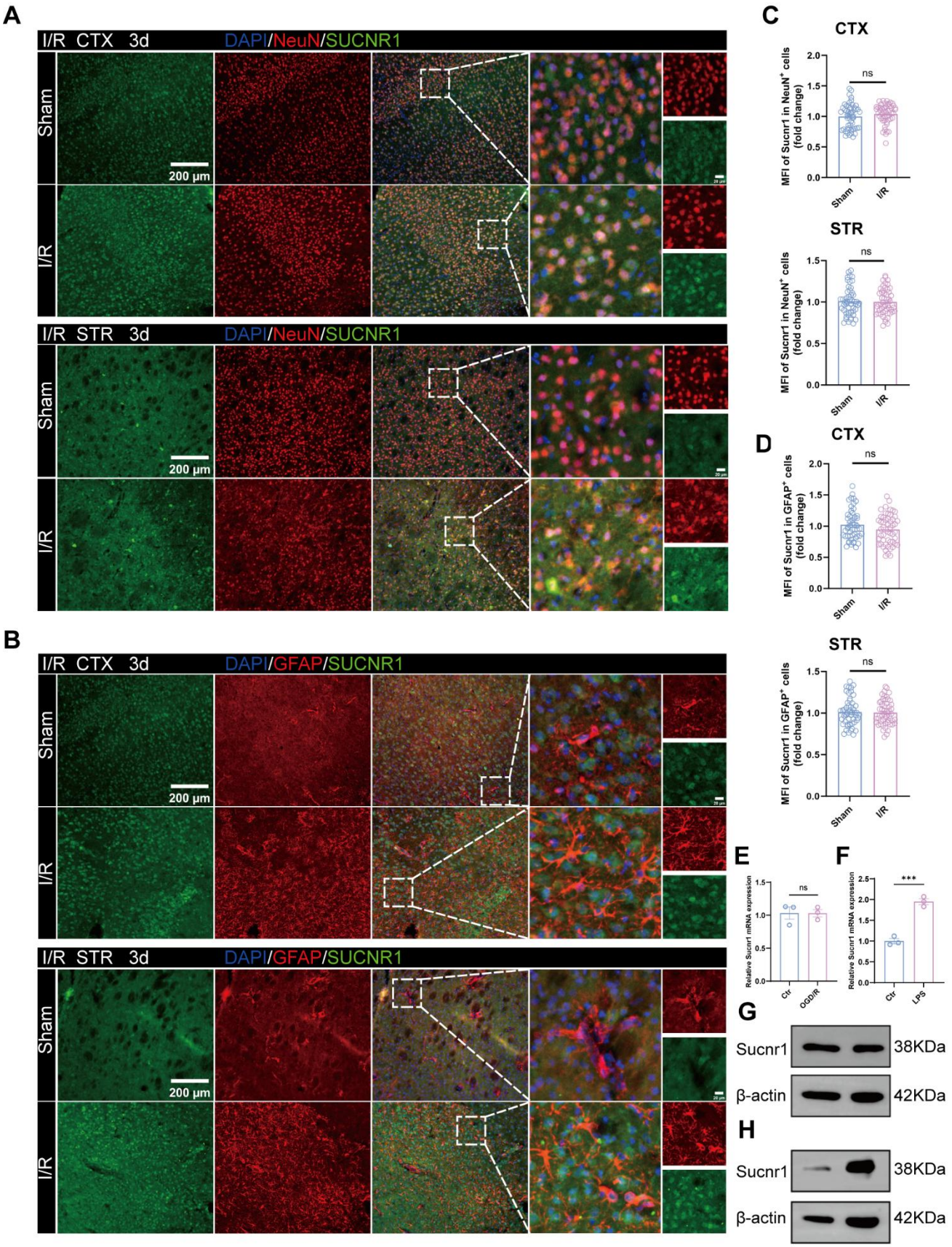


Figure S5. Sucnr1 expression in neurons and astrocytes after acute stroke and under different treatments in vitro.

(a) Representative immunofluorescence images showing colocalization of Sucnr1 with the neuronal marker NeuN in the cortex and striatum of Sham and I/R mice. Low- and high-magnification views are presented, with scale bars = 200 μm and 20 μm, respectively.
(b) Immunofluorescence staining showing Sucnr1 expression in astrocytes in the cortical and striatal regions of Sham and I/R mice. Scale bars = 200 μm and 20 μm.
(c) Quantification of Sucnr1 fluorescence intensity in $NeuN^+$ neurons within the ipsilateral cortex and striatum at day 3 after I/R (n > 50 cells per group).
(d) Quantification of Sucnr1 fluorescence intensity in astrocytes in the ipsilateral cortex and striatum at day 3 after I/R (n > 50 cells per group).
(e, f) qPCR and **(g, h)** Western blot analyses were performed to detect the expression levels of Sucnr1 in microglia under different treatment conditions, with n = 3 per group. Data are presented as mean ± SEM. Comparisons between groups were performed using an unpaired two-tailed Student's *t*-test. ***p < 0.001, ns = not significant.

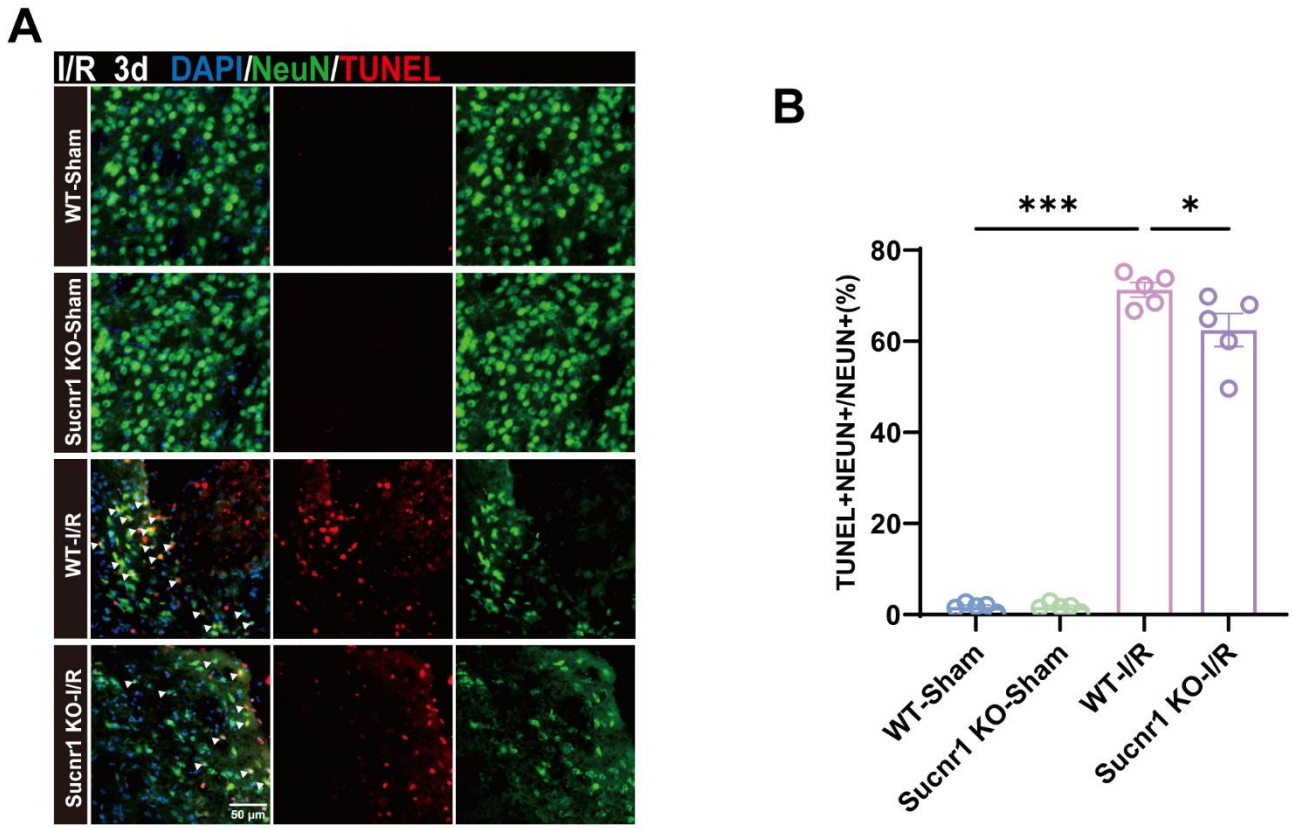


Figure S6.TUNEL staining reveals neuronal apoptosis in the ipsilateral striatum after acute stroke.
(a) Representative immunofluorescence images of the ipsilateral striatum showing colocalization of NeuN, a neuronal marker, with TUNEL, an apoptosis marker, to evaluate neuronal apoptosis. Scale bar = 50 μm.
(b) Quantification of apoptotic neurons, expressed as the percentage of $NeuN^+/TUNEL^+$ cells in each group (n = 5 per group).Data are presented as mean ± SEM. Statistical analyses were performed using one-way or two-way ANOVA followed by Tukey's post hoc test.*p < 0.05, ***p < 0.001.

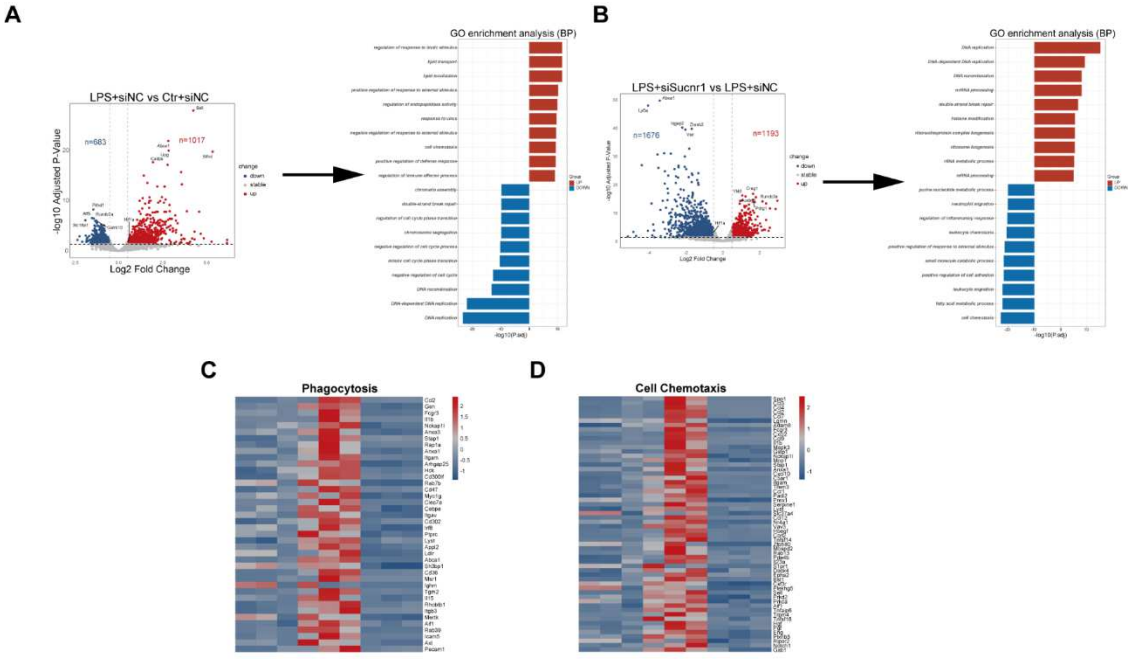


Figure S7. Transcriptomic pathway alterations after Sucnr1 knockdown in microglia.

(a) Volcano plot and bar graph showing differentially expressed genes (DEGs) in LPS-stimulated microglia (LPS+siNC) compared with control (Ctrl+siNC), along with Gene Ontology (GO) pathway enrichment analysis of these DEGs.

(b) Volcano plot and GO enrichment analysis of DEGs in the LPS+siSucnr1 group compared with the LPS+siNC group, reflecting transcriptomic changes following Sucnr1 knockdown. DEGs were defined by $|\log_2 FC| > 1$ and adjusted *P* (P adj.) < 0.05 (n = 3).

(c, d) Heatmaps depicting the expression patterns of genes related to phagocytic function and cell migration across the three groups.

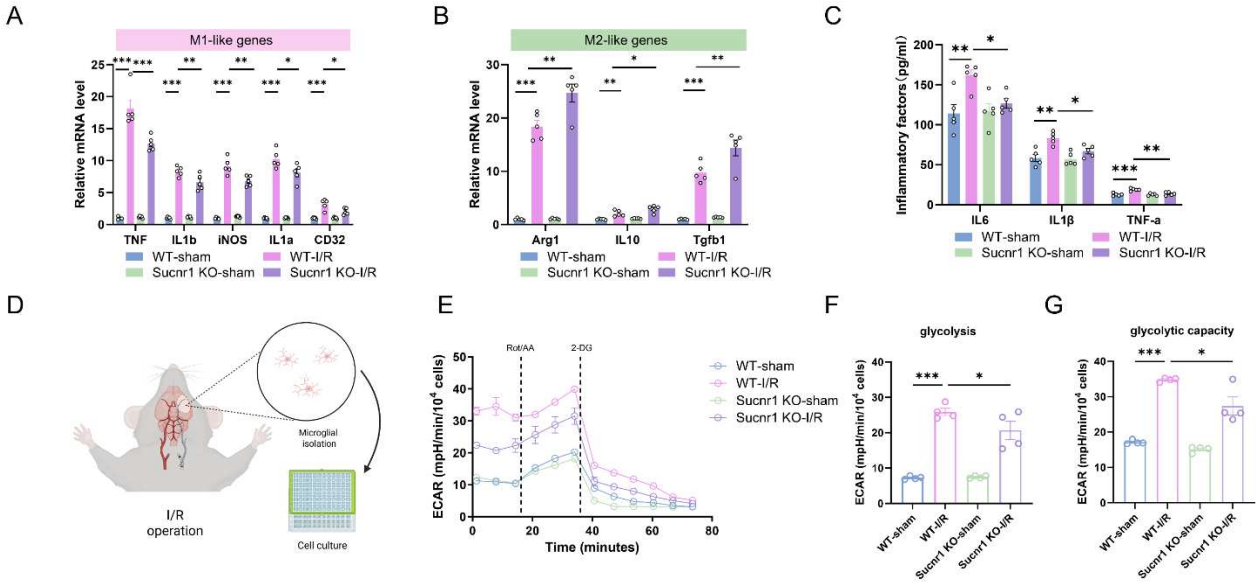


Figure S8. Sucnr1 deletion attenuates microglial polarization and metabolic reprogramming after acute stroke.

(a) qPCR analysis of mRNA expression levels of M1-like microglial pro-inflammatory markers, including TNF-α, IL-1β, iNOS, IL-1α, and CD32, in the ipsilateral cortex of WT-sham, WT-I/R, Sucnr1 KO-sham, and Sucnr1 KO-I/R mice.

(b) qPCR assessment of M2-like microglial anti-inflammatory markers, including Arg1, IL-10, and TGF-β1, in the same groups.

(c) ELISA quantification of IL-6, IL-1β, and TNF-α protein levels in brain tissue homogenates.

(d) Schematic illustration of the experimental workflow (created with BioRender): $CD11b^{+}$ microglia were isolated using magnetic beads, followed by analysis of extracellular acidification rate (ECAR) using a Seahorse XF analyzer.

(e) Real-time ECAR profiles obtained by Seahorse XF analysis, reflecting dynamic changes in glycolytic activity in microglia from each group (n = 4).

(f) Quantification of basal glycolysis based on ECAR measurements (n = 4).

(g) Quantification of glycolytic capacity in microglia from the indicated groups (n = 4).

Data are presented as mean ± SEM. Statistical analyses were performed using one-way or two-way ANOVA followed by Tukey's post hoc test.*p < 0.05, **p < 0.01, **p < 0.001.

Supplementary Files

This is a list of supplementary files associated with this preprint. Click to download.

- qPCRprimerstablesupportarytable1.xlsx
- wbraw.pdf